

A least-squares meshfree method for the incompressible Navier–Stokes equations: A satisfactory solenoidal velocity field via a staggered-variable arrangement

Takeharu Matsuda ^a and Satoshi Ii *^a

^a *Department of Mechanical Engineering, School of Engineering, Institute of Science Tokyo, 2-12-1 Ookayama, Meguro-ku, Tokyo 152-8550, Japan*

Abstract

Incompressible flow solvers based on strong-form meshfree methods represent arbitrary geometries without the need for a global mesh system. However, their local evaluations make it difficult to satisfy incompressibility at the discrete level. Moreover, the collocated arrangement of velocity and pressure variables tends to induce a zero-energy mode, leading to decoupling between the two variables. In projection-based approaches, a spatial discretization scheme based on a conventional node-based moving least-squares method for the pressure causes inconsistency between the discrete operators on both sides of the Poisson equation. Thus, a solenoidal velocity field cannot be ensured numerically. In this study, a numerical method for the incompressible Navier–Stokes equations is developed by introducing a local primal–dual grid into the mesh-constrained discrete point method, enabling consistent discrete operators. The *virtual* dual cell constructed is based on the local connectivity among nodes, and therefore our method remains truly meshfree. To achieve a consistent coupling between velocity and pressure variables under the primal–dual arrangement, time evolution converting is applied to evolve the velocity on cell interfaces. For numerical validation, a linear acoustic equation is solved to confirm the effectiveness of the staggered-variable arrangement based on the local primal–dual grid. Then, incompressible Navier–Stokes equations are solved, and the proposed method is demonstrated to satisfy the condition of a solenoidal velocity field at the discrete level, achieve the expected spatial convergence order, and accurately reproduce flow features over a wide range of Reynolds numbers.

Keywords: least-squares meshfree/meshless method, staggered-variable arrangement, computational fluid dynamics, incompressible Navier–Stokes equations, velocity–pressure coupling, mesh-constrained discrete point method

1 Introduction

Meshfree/meshless methods are a class of numerical methods that represent the computational domain using discrete points (DPs), and have been developed to simulate practical problems without the time-consuming and labor-intensive process of mesh generation. Broadly, there are two types of meshfree methods. One is based on weak formulations, such as the element-free Galerkin method [1, 2], the meshless local Petrov–Galerkin method [3, 4], and reproducing kernel particle method [5]. The other type is based on strong formulations, such as the smoothed particle hydrodynamics (SPH) [6], the moving particle semi-implicit/simulation method [7], the finite-point method [8], and the generalized finite-difference method

*Corresponding author.

Email addresses: matsuda.t.52ec@m.isct.ac.jp (Takeharu Matsuda , ii.s.148c@m.isct.ac.jp (Satoshi Ii 

[9, 10, 11, 12, 13]. The latter, strong-form meshfree methods, are considered truly meshfree because the governing equations are evaluated locally, thereby inherently avoiding use of global mesh structures.

Recently, incompressible flow solvers based on strong-form meshfree methods have been proposed [14, 15, 16, 17, 18, 19, 20]. These use moving least-squares (MLS)[21] for spatial discretization and Taylor series consistency. Moreover, improved methods with more accurate higher-order temporal convergence have been developed [22, 23], and meshfree methods have shown increased usefulness in practice. However, these strong-form meshfree methods for incompressible flows tend to suffer from unphysical checkerboard instability on flow fields, which arises from a zero-energy mode associated with the collocated arrangement of velocity and pressure variables. This makes it difficult to achieve the expected order of spatial convergence for both velocity and pressure. The problem of zero-energy pressure modes has been known for a long time in mesh-based methods such as the finite difference, finite element, and finite volume methods. This problem is due to the collocated arrangement of velocity and pressure variables. In such cases, the pressure gradient and velocity are evaluated at inconsistent positions, which allows a nonphysical checkerboard pressure distribution [24]. In the framework of meshfree methods, Swegle *et al.* first reported the zero-energy mode problem in the context of SPH [25]. The zero-energy mode is also reported to enhance tensile instability under negative pressure or strong vortices [26], and it is one of the difficult issues in meshfree methods.

Several improved meshfree schemes have been proposed, such as evaluating stresses at staggered positions relative to velocity points, and they have been effective in structural analysis [27, 28, 29]. Moreover, some formulations for incompressible flows introduce staggered particles at every time step so that velocity and pressure can be arranged in a staggered manner. He *et al.* proposed staggered SPH methods that evaluate the momentum and pressure gradient at the midpoints between particles and avoid the zero-energy mode [30, 31]. The existence and stability of solutions to the meshfree methods introducing such a virtual staggered point have been proved by Park *et al.* [32]. However, these approaches assume a uniform particle arrangement. Liu *et al.* proposed a stable staggered particle method that generates evaluation points for pressure at every time step based on vertices of uniform Euler grids [26]. As a trade-off for the stability, this approach increases the computational cost owing to the virtual pressure points. In addition, Trask *et al.* [33] have proposed a high-order staggered meshless method for elliptic boundary value problems that locally defines a virtual cell for each discrete point. This is motivated by the primal–dual relationship between cell-centered and cell-interface quantities in the finite volume method, and it enables consistent evaluation of discrete gradient and divergence operators in a truly meshfree manner. This method has also been extended to Stokes flow [34]. However, to our knowledge, no strong-form meshfree method exists for incompressible flows that can satisfy the requirement of a divergence-free velocity field at the discrete level.

In this study, we propose a strong-form meshfree method for the incompressible Navier–Stokes equations. Velocity and pressure are coupled using the fractional step method (or pressure projection method) [35]. The proposed method is based on the local primal–dual grid introduced by Trask *et al.* [33] and allows a divergence-consistent MLS reconstruction with radial components for spatial discretization, which enables use of compatible discrete gradient and divergence operators. Because of this property, the method achieves a solenoidal velocity field on the order of the residual norm of the linear system for the pressure Poisson equation. The pressure Poisson equation is solved in a staggered manner using the radial component of the velocity evaluated on virtual dual-cell interfaces. In this framework, a time-evolution converting (TEC) formula [36, 37, 38] is applied to update the radial component of the velocity at the virtual dual-cell interface with temporal information on the flow, and this time-evolved quantity is then used to obtain the pressure field. Although the TEC formula differs from momentum-based interpolation (e.g., [39, 40]), it provides a strong coupling between velocity and pressure by temporally linking the two variables. The proposed method extends the mesh-constrained discrete point (MCD) method, which is a type of strong-form meshfree method. The MCD method has been developed as an efficient solver for incompressible flows with arbitrary boundaries [19], and it has already been extended to moving boundary problems [20]. In the MCD method, DPs are associated one-to-one with each mesh element of a structured mesh system (background mesh), which is laid over the analysis domain. Each DP can be arbitrarily located inside its associated background mesh element, but it cannot exist outside of the cell boundary. This is so-called mesh constraint. By arranging DPs along arbitrary boundary shapes under this mesh constraint, the method can realize both a faithful geometrical representation with DPs and efficient memory access using index information from the background mesh. This discrete representation provides a uniform DP distribution at the level of the background mesh, and a constant stencil size can be expected. Therefore, a second-order spatial discretization based on MLS can be

stably evaluated with a compact 3×3 stencil. The background mesh is used only for the mesh constraint and not for flow calculation or Gaussian integration, which makes the method different from existing mesh–particle hybrid methods (e.g., [41, 42, 43, 44, 45, 46, 47]).

This paper contains the following sections. In Section 2, the fundamental formulation of the proposed method, comprising the spatial discretization scheme and velocity–pressure coupling method, is described. Section 3 compares results obtained with the proposed methods with those of an existing meshfree method using the collocated variable arrangement, and investigates the effectiveness of the staggered-variable arrangement in the meshfree framework and applicability to incompressible Navier–Stokes flows. In Section 4, the conclusion and remarks are given.

2 A meshfree incompressible flow solver with consistent velocity–pressure coupling

2.1 Overview

In this study, an incompressible flow solver is developed on the basis of the MCD method [19, 20]. The spatial discretization scheme is based on MLS reconstruction with radial components [33, 34], and spatial derivatives are evaluated using 3×3 compact stencils. The MLS scheme satisfies Taylor series consistency, and settings such as the polynomial basis, scaling parameter, and influence radius are set as in [20].

Section 2.2 explains the MLS reconstruction based on the radial components of quantities. Section 2.3 introduces the spatial discretization scheme constructed using the local primal–dual arrangement. Section 2.4 describes the treatment of boundary conditions in the MLS reconstruction with radial components. Section 2.5 describes the basic concept of the proposed staggered formulation for coupling the velocity and pressure, where a linear acoustic equation is used as an essential example. Section 2.6 presents the numerical solver for the unsteady incompressible Navier–Stokes equations based on the pressure projection method.

2.2 MLS reconstruction using radial components

As in [33], a vector variable $\mathbf{u}(\mathbf{x})$ in $\mathbf{x} \in \mathbb{R}^d$, where d is the dimension number ($d = 1, 2, 3$), is converted to a radial component from a point \mathbf{x}_c , $U_{c \rightarrow}(\mathbf{x}) \in \mathbb{R}^1$:

$$U_{c \rightarrow}(\mathbf{x}) = 2(\mathbf{x} - \mathbf{x}_c) \cdot \mathbf{u}(\mathbf{x}). \quad (1)$$

Here, the following relations hold:

$$\nabla U_{c \rightarrow}(\mathbf{x}) = 2\mathbf{u}(\mathbf{x}) + 2\nabla\mathbf{u}(\mathbf{x}) \cdot (\mathbf{x} - \mathbf{x}_c), \quad (2)$$

$$\rightarrow \quad \nabla U_{c \rightarrow}(\mathbf{x}_c) = 2\mathbf{u}(\mathbf{x}_c), \quad (3)$$

$$\nabla\nabla U_{c \rightarrow}(\mathbf{x}) = 2\nabla\mathbf{u}(\mathbf{x}) + 2(\nabla\mathbf{u}(\mathbf{x}))^\top + 2\nabla\nabla\mathbf{u}(\mathbf{x}) \cdot (\mathbf{x} - \mathbf{x}_c), \quad (4)$$

$$\rightarrow \quad \nabla\nabla U_{c \rightarrow}(\mathbf{x}_c) = 2\nabla\mathbf{u}(\mathbf{x}_c) + 2(\nabla\mathbf{u}(\mathbf{x}_c))^\top, \quad (5)$$

and

$$\nabla^2 U_{c \rightarrow}(\mathbf{x}) = 4\nabla \cdot \mathbf{u}(\mathbf{x}) + 2\nabla^2 \mathbf{u}(\mathbf{x}) \cdot (\mathbf{x} - \mathbf{x}_c), \quad (6)$$

$$\rightarrow \quad \nabla^2 U_{c \rightarrow}(\mathbf{x}_c) = 4\nabla \cdot \mathbf{u}(\mathbf{x}_c). \quad (7)$$

A local polynomial function $U_c^h(\mathbf{x}) = \mathbf{c}_c \cdot \mathbf{p}_c(\mathbf{x})$ is introduced as an approximate function of $U_{c \rightarrow}(\mathbf{x})$, where the components of \mathbf{c}_c are the coefficients and $\mathbf{p}_c(\mathbf{x})$ is the arbitrary order basis function, which is reconstructed by solving the optimization problem

$$\operatorname{argmin}_{\mathbf{c}_c} \frac{1}{2} \sum_{\mathbf{x} \in \Omega_c} w_c(\mathbf{x}) (U_c^h(\mathbf{x}) - U_{c \rightarrow}(\mathbf{x}))^2, \quad (8)$$

where $w_c(\mathbf{x})$ is the weight function from \mathbf{x}_c .

Thus, once the approximate function $U_c^h(\mathbf{x})$ is reconstructed, the spatial derivatives at \mathbf{x}_c are approximated as

$$\mathbf{u}(\mathbf{x}_c) \approx \mathbf{u}^h(\mathbf{x}_c) = \frac{1}{2} \nabla U_c^h(\mathbf{x}_c), \quad (9)$$

$$\nabla \cdot \mathbf{u}(\mathbf{x}_c) \approx \nabla \cdot \mathbf{u}^h(\mathbf{x}_c) = \frac{1}{4} \nabla^2 U_c^h(\mathbf{x}_c), \quad (10)$$

where \mathbf{u}^h is the approximate function of \mathbf{u} .

These formulae can be extended to the tensor variables such as by approximating $\nabla \cdot \boldsymbol{\sigma}$, where $\boldsymbol{\sigma} \in \mathbb{R}^{d \times d}$ is a second-order tensor (e.g., Cauchy stress tensor). For a second-order tensor, polynomials are reconstructed for a vector quantity in the radial projection $\boldsymbol{\Sigma}_c^h(\mathbf{x}) = 2(\mathbf{x} - \mathbf{x}_c) \cdot \boldsymbol{\sigma}(\mathbf{x}) \in \mathbb{R}^d$, and $\nabla \cdot \boldsymbol{\sigma}$ is approximated as

$$\nabla \cdot \boldsymbol{\sigma}(\mathbf{x}_c) \approx \nabla \cdot \boldsymbol{\sigma}^h(\mathbf{x}_c) = \frac{1}{4} \nabla^2 \boldsymbol{\Sigma}_c^h(\mathbf{x}_c). \quad (11)$$

2.3 Spatial discretization with a local primal–dual arrangement

In this study, the primal–dual arrangement [33] is developed for MLS reconstruction with radial components (Fig. 1). The domain Ω is discretized using a set of non-overlapping DP nodes (or vertices) $\mathcal{V} = \{v_i\}_{i=1}^{N_{\text{DP}}}$, where each position is given as $\{\mathbf{x}_i\}_{i=1}^{N_{\text{DP}}}$. A set of local nodes \mathcal{V}_i is introduced in the MCD framework as

$$\mathcal{V}_i = \{v_j \in \mathcal{V} \mid \mathbf{x}_j \in \mathcal{D}_i\}, \quad (12)$$

where \mathcal{D}_i denotes a compact support domain for the node v_i associated with the 3×3 background mesh, and a set of local edges \mathcal{E}_i is introduced as

$$\mathcal{E}_i = \{e_{ij} = \{v_i, v_j\} \mid v_j \in \mathcal{V}_i \text{ and } v_i \neq v_j\}, \quad (13)$$

where e_{ij} denotes the edge, which links v_i to v_j . The local primal–dual grid associated with v_i is then given by $\mathcal{G}_i(\mathcal{V}_i, \mathcal{E}_i)$ as a local graph consisting of \mathcal{V}_i and \mathcal{E}_i in Eqs. (12) and (13), respectively. Regarding the local primal–dual grid, a virtual dual cell c_i is introduced for each node v_i . The boundary of c_i consists of a virtual face f_{ij} ($\cap f_{ij} = \partial c_i$), where each face intersects the edge e_{ij} with a unit normal vector $\hat{\mathbf{m}}_{ij}$ parallel to the edge vector $\mathbf{e}_{ij} = \mathbf{x}_j - \mathbf{x}_i$ on e_{ij} for the local primal–dual grid. The intersection point \mathbf{x}_{ij} between the edge e_{ij} and face f_{ij} can be arbitrarily defined as

$$\mathbf{x}_{ij} = (1 - \theta_{ij})\mathbf{x}_i + \theta_{ij}\mathbf{x}_j, \quad (14)$$

where $\theta_{ij} \in (0, 1]$ denotes an arbitrary parameter for determining the intersection point \mathbf{x}_{ij} . In this study, we set the parameter to

$$\theta_{ij} = 1/2, \quad (15)$$

with $\mathbf{x}_{ij} = (\mathbf{x}_i + \mathbf{x}_j)/2$ as the middle point of the edge e_{ij} . A set of edges f_{ij} for the cell c_i is defined as

$$\mathcal{F}_i = \{f_{ij} \in \partial c_i \mid \mathbf{x}_{ij} \text{ on } e_{ij} \text{ and } \hat{\mathbf{m}}_{ij} \parallel \mathbf{e}_{ij}\}. \quad (16)$$

It should be noted that, as in [33], the present study introduces a *virtual* dual cell, which is based on the local connectivity of nodes, rather than a *physical* one. Therefore, the explicit geometric dimensions of the dual cell c_i and its faces f_{ij} are not required.

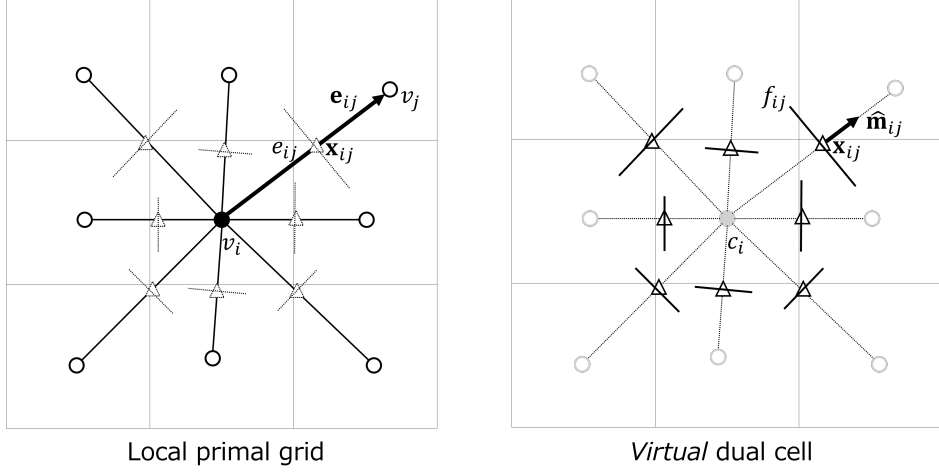


Figure 1: Illustrations of the local primal grid (left) and *virtual* dual cell (right).

By applying the primal–dual arrangement, we can express the radial component of the velocity $\mathbf{u}(\mathbf{x})$ at each intersection point \mathbf{x}_{ij} as

$$U_{i \rightarrow ij} = U_{i \rightarrow}(\mathbf{x}_{ij}) = 2(\mathbf{x}_{ij} - \mathbf{x}_i) \cdot \mathbf{u}_{ij}, \quad (17)$$

where $\mathbf{u}_{ij} = \mathbf{u}(\mathbf{x}_{ij})$. When an approximate polynomial function $U_i^h(\mathbf{x})$ of $U_{i \rightarrow}(\mathbf{x}) = 2(\mathbf{x} - \mathbf{x}_i) \cdot \mathbf{u}(\mathbf{x})$ is introduced for a node v_i (or cell c_i) at \mathbf{x}_i , U_i^h can be approximated by the MLS reconstruction using $U_{i \rightarrow ij}$:

$$\operatorname{argmin}_{\mathbf{c}_i} \frac{1}{2} \sum_{\mathbf{x}_{ij} \text{ on } \mathcal{F}_i} w_i(\mathbf{x}_{ij}) (U_i^h(\mathbf{x}_{ij}) - U_{i \rightarrow ij})^2, \quad (18)$$

where the components of \mathbf{c}_i are the coefficients of polynomial function $U_i^h(\mathbf{x})$. Consequently, spatial derivatives at \mathbf{x}_i are obtained as

$$\mathbf{u}^h(\mathbf{x}_i) = \frac{1}{2} \nabla U_i^h(\mathbf{x}_i), \quad (19)$$

$$\nabla \cdot \mathbf{u}^h(\mathbf{x}_i) = \frac{1}{4} \nabla^2 U_i^h(\mathbf{x}_i). \quad (20)$$

2.4 Treatment of boundary conditions on a primal–dual arrangement

We extend the formulation using the primal–dual arrangement in the case that a normal component of any quantity is imposed as a boundary condition on the boundary Γ_d . The set of edges \mathcal{F}_i in (16) is decomposed into two sets, one that includes Γ_d and one that does not:

$$\mathcal{F}_i^{(d)} = \{f_{ij} \in \partial c_i \mid \mathbf{x}_{ij} \text{ on } e_{ij}, \hat{\mathbf{m}}_{ij} = \mathbf{n}_j, \mathbf{x}_j \in \Gamma_d\}, \quad (21)$$

$$\tilde{\mathcal{F}}_i = \{f_{ij} \in \partial c_i \mid \mathbf{x}_{ij} \text{ on } e_{ij}, \hat{\mathbf{m}}_{ij} \parallel \mathbf{e}_{ij}, \mathbf{x}_j \notin \Gamma_d\}, \quad (22)$$

where \mathbf{n}_j is the unit normal vector at \mathbf{x}_j on the boundary Γ_d .

Assuming that the neighboring node $v_j \in \mathcal{V}_i$ is located on the boundary Γ_d , the normal projection of $\mathbf{u}^h(\mathbf{x}_{ij})$ is given by approximating Eq. (2) as

$$\mathbf{n}_j \cdot \mathbf{u}^h(\mathbf{x}_{ij}) = \frac{1}{2} \partial_n U_i^h(\mathbf{x}_{ij}) + \mathcal{O}(\|\mathbf{x}_j - \mathbf{x}_i\|) \approx \frac{1}{2} \partial_n U_i^h(\mathbf{x}_{ij}), \quad (23)$$

where $\partial_n = \mathbf{n}_j \cdot \nabla$ denotes the normal derivative operator (Fig. 2).

Using Eq. (23) to impose a boundary condition $q_{ij} \approx q_j = \mathbf{n}_j \cdot \mathbf{u}_j$ on Γ_d , we then extend Eq. (18) as

$$\operatorname{argmin}_{\mathbf{c}_i} \frac{1}{2} \sum_{\mathbf{x}_{ij} \text{ on } \tilde{\mathcal{F}}_i} w_i(\mathbf{x}_{ij}) (U_i^h(\mathbf{x}_{ij}) - U_{i \rightarrow ij})^2 + \frac{1}{2} \sum_{\mathbf{x}_{ij} \text{ on } \mathcal{F}_i^{(d)}} r_s w_i(\mathbf{x}_j) (\partial_n U_i^h(\mathbf{x}_{ij}) - 2q_j)^2, \quad (24)$$

where $q_j = q(\mathbf{x}_j)$ and r_s denotes the scaling parameter. The second term of Eq. (24) reflects the boundary condition, which is inspired by the formulation that applies the Neumann condition for U_i^h proposed in [17].

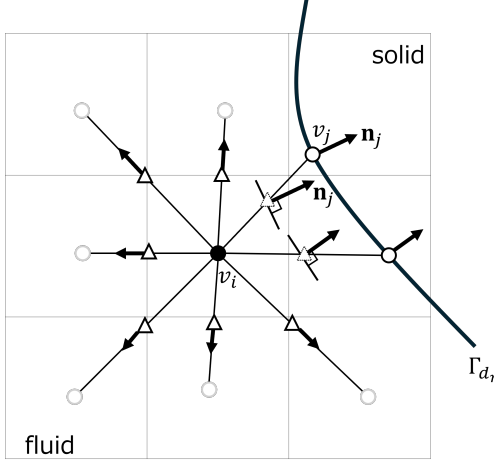


Figure 2: Illustration of applying the normal component of any vector (or tensor) quantity as a boundary condition on Γ_{d_n} .

2.5 Formulation of the linear acoustic equation

We formulate the coupling of the velocity and pressure in the staggered-variable arrangement for a linear acoustic equation. The governing equations are expressed as

$$\frac{\partial p}{\partial t} = -\rho c^2 \nabla \cdot \mathbf{u}, \quad (25)$$

$$\rho \frac{\partial \mathbf{u}}{\partial t} = -\nabla p, \quad (26)$$

where $\partial/\partial t$ and $\nabla = \partial/\partial \mathbf{x}$ denote the temporal and spatial derivative operators, respectively. c denotes the acoustic speed, ρ denotes the fluid density, and \mathbf{u} and p denote the velocity and pressure.

These equations are discretized using the staggered arrangement of velocity and pressure variables based on the local primal–dual grids (Fig. 3). While the pressure is defined on each DP, the radial component $U_{i \rightarrow ij} = 2(\mathbf{x}_{ij} - \mathbf{x}_i) \cdot \mathbf{u}(\mathbf{x}_{ij})$ of the velocity is given on each midpoint \mathbf{x}_{ij} of the edge vector \mathbf{e}_{ij} (i.e., a staggered point). According to the variable arrangement of velocity and pressure, the semi-discrete forms of Eqs. (25) and (26) can be written as

$$\frac{p_i^{n+1} - p_i^n}{\Delta t} = -\rho c^2 \nabla \cdot \mathbf{u}|_i^n = -\frac{\rho c^2}{4} \nabla^2 U_i^h|_i^n, \quad (27)$$

$$\rho \frac{U_{i \rightarrow ij}^{n+1} - U_{i \rightarrow ij}^n}{\Delta t} = -2(\mathbf{x}_{ij} - \mathbf{x}_i) \cdot \nabla p|_{ij}^{n+1}. \quad (28)$$

In this study, we apply the second-order approximation for the MLS reconstruction of $U_i^h(\mathbf{x})$ and the radial projection of the pressure gradient on the right side of Eq. (28). The Taylor series expansions of $p(\mathbf{x}_i)$ and $p(\mathbf{x}_j)$ corresponding to the midpoint \mathbf{x}_{ij} can be written as

$$p(\mathbf{x}_i) = p(\mathbf{x}_{ij}) + (\mathbf{x}_i - \mathbf{x}_{ij}) \cdot \nabla p|_{ij} + \mathcal{O}(\|\mathbf{e}_{ij}\|^2), \quad (29)$$

$$p(\mathbf{x}_j) = p(\mathbf{x}_{ij}) + (\mathbf{x}_j - \mathbf{x}_{ij}) \cdot \nabla p|_{ij} + \mathcal{O}(\|\mathbf{e}_{ij}\|^2). \quad (30)$$

By subtracting Eq. (30) from Eq. (29), we obtain the pressure gradient as

$$(\mathbf{x}_j - \mathbf{x}_i) \cdot \nabla p|_{ij} = 2(\mathbf{x}_{ij} - \mathbf{x}_i) \cdot \nabla p|_{ij} = p_j - p_i + \mathcal{O}(\|\mathbf{e}_{ij}\|^2). \quad (31)$$

Thus, Eq. (28) can be approximated by

$$\rho \frac{U_{i \rightarrow ij}^{n+1} - U_{i \rightarrow ij}^n}{\Delta t} = -(p_j^{n+1} - p_i^{n+1}). \quad (32)$$

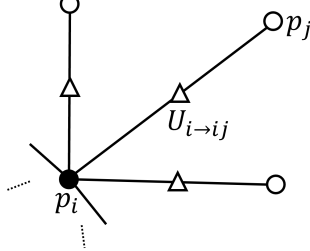


Figure 3: Staggered-variable arrangement for the 2D linear acoustic equation on local primal–dual grids.

2.6 Formulation of the incompressible Navier–Stokes equations

The proposed formulation is applied to the incompressible Navier–Stokes equations given in the following conservative form:

$$\nabla \cdot \mathbf{u} = 0, \quad (33)$$

$$\frac{\partial(\rho \mathbf{u})}{\partial t} + \nabla \cdot (\rho \mathbf{u} \mathbf{u}) = -\nabla p + \nabla \cdot \boldsymbol{\tau}, \quad (34)$$

where ρ denotes the fluid density, \mathbf{u} and p denote the velocity and pressure, and $\boldsymbol{\tau} = \eta (\nabla \mathbf{u} + (\nabla \mathbf{u})^\top)$ denotes the viscous stress tensor. According to Eq. (33), the viscous term can be written as $\nabla \cdot \boldsymbol{\tau} = \eta \nabla \cdot \nabla \mathbf{u}$. Assuming a constant density ($\rho = \text{const.}$), Eq. (34) can be rewritten as

$$\rho \left(\frac{\partial \mathbf{u}}{\partial t} + \nabla \cdot (\mathbf{u} \mathbf{u}) \right) = -\nabla p + \eta \nabla \cdot \nabla \mathbf{u}. \quad (35)$$

Applying the pressure projection method with the first-order explicit method, we can express the semi-discrete forms of Eqs. (33) and (35) as

$$\rho \left(\frac{\mathbf{u}_i^* - \mathbf{u}_i^n}{\Delta t} + \nabla \cdot (\mathbf{u}^n \mathbf{u}^n) \big|_i \right) = \eta \nabla \cdot \nabla \mathbf{u}^n \big|_i, \quad (36)$$

$$U_{i \rightarrow ij}^* = \text{TEC} (U_{i \rightarrow ij}^n, \mathbf{u}_i^n, \mathbf{u}_j^n, \mathbf{u}_i^*, \mathbf{u}_j^*), \quad (37)$$

$$\nabla \cdot \nabla p^{n+1} \big|_i = \frac{\rho}{\Delta t} \nabla \cdot \mathbf{u}^* \big|_i, \quad (38)$$

$$\rho \frac{U_{i \rightarrow ij}^{n+1} - U_{i \rightarrow ij}^*}{\Delta t} = 2(\mathbf{x}_{ij} - \mathbf{x}_i) \cdot \nabla p^{n+1} \big|_{ij}, \quad (39)$$

$$\rho \frac{\mathbf{u}_i^{n+1} - \mathbf{u}_i^*}{\Delta t} = -\nabla p^{n+1} \big|_i. \quad (40)$$

Fig. 4 illustrates staggered arrangements of p_i , \mathbf{u}_i , and $U_{i \rightarrow ij}$. When the MLS reconstruction is applied with local primal–dual grids, the following radial components are defined:

$$U_{i \rightarrow ij} = 2(\mathbf{x}_{ij} - \mathbf{x}_i) \cdot \mathbf{u} \big|_{ij}, \quad (41)$$

$$\delta P_{i \rightarrow ij} = 2(\mathbf{x}_{ij} - \mathbf{x}_i) \cdot \nabla p \big|_{ij}, \quad (42)$$

$$\mathbf{A}_{i \rightarrow ij} = 2(\mathbf{x}_{ij} - \mathbf{x}_i) \cdot (\mathbf{u} \mathbf{u}) \big|_{ij}, \quad (43)$$

$$\mathbf{D}_{i \rightarrow ij} = 2(\mathbf{x}_{ij} - \mathbf{x}_i) \cdot \nabla \mathbf{u} \big|_{ij}. \quad (44)$$

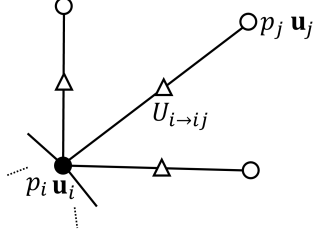


Figure 4: Staggered-variable arrangement for the 2D Navier–Stokes equations on local primal–dual grids.

When these definitions are used, the prediction step for the intermediate velocity \mathbf{u}^* [Eq. (36)] can be expressed as

$$\rho \left(\frac{\mathbf{u}_i^* - \mathbf{u}_i^n}{\Delta t} + \frac{1}{4} \nabla^2 \mathbf{A}_i^h \big|_i^n \right) = \frac{1}{4} \eta \nabla^2 \mathbf{D}_i^h \big|_i^n. \quad (45)$$

Here, $\mathbf{A}_{i \rightarrow ij}$ is approximated with an upwind technique:

$$\mathbf{A}_{i \rightarrow ij} = \begin{cases} U_{i \rightarrow ij} \mathbf{u}_i^h \big|_{ij}, & \text{for } U_{i \rightarrow ij} \geq 0, \\ U_{i \rightarrow ij} \mathbf{u}_j^h \big|_{ij}, & \text{otherwise,} \end{cases} \quad (46)$$

where $\mathbf{u}_i^h \big|_{ij} = \mathbf{u}_i^h(\mathbf{x}_{ij})$ or $\mathbf{u}_j^h \big|_{ij} = \mathbf{u}_j^h(\mathbf{x}_{ij})$ denotes the polynomial approximations of velocities at \mathbf{x}_{ij} from \mathbf{x}_i or \mathbf{x}_j . These interpolations are carried out using the standard nodal-based MLS scheme (not local primal–dual grids) at nodes v_i and v_j , as described in [19, 20]. The pressure–projection parts [Eqs. (38)–(40)] can be expressed as

$$\nabla^2 \delta P_i^h \big|_i^{n+1} = \frac{\rho}{\Delta t} \nabla^2 U_i^h \big|_i^*, \quad (47)$$

$$\rho \frac{U_{i \rightarrow ij}^{n+1} - U_{i \rightarrow ij}^*}{\Delta t} = -\delta P_{i \rightarrow ij}^{n+1}, \quad (48)$$

$$\rho \frac{\mathbf{u}_i^{n+1} - \mathbf{u}_i^*}{\Delta t} = -\frac{1}{2} \nabla \delta P_i^h \big|_i^{n+1}. \quad (49)$$

In a procedure analogous to that for the linear acoustic equation, the second-order approximation [33] is employed:

$$\delta P_{i \rightarrow ij} = p_j - p_i, \quad (50)$$

$$\mathbf{D}_{i \rightarrow ij} = \mathbf{u}_j - \mathbf{u}_i. \quad (51)$$

The TEC formula [36, 37, 38] is based on the following concept:

$$\frac{\partial U_{i \rightarrow ij}}{\partial t} = \frac{1}{2} \left(\frac{\partial \mathbf{U}_i^h \big|_{ij}}{\partial t} + \frac{\partial \mathbf{U}_j^h \big|_{ij}}{\partial t} \right), \quad (52)$$

where $\mathbf{U}_i^h \big|_{ij} = 2(\mathbf{x}_{ij} - \mathbf{x}_i) \cdot \mathbf{u}_i^h \big|_{ij}$ and $\mathbf{U}_j^h \big|_{ij} = 2(\mathbf{x}_{ij} - \mathbf{x}_j) \cdot \mathbf{u}_j^h \big|_{ij}$ are the radial components of the interpolated velocities $\mathbf{u}_i^h(\mathbf{x}_{ij})$ and $\mathbf{u}_j^h(\mathbf{x}_{ij})$ from the nodes v_i and v_j , respectively. Applying the first-order method for discretizing Eq. (52), we can write Eq. (37) as

$$\begin{aligned} \text{TEC} (U_{i \rightarrow ij}^n, \mathbf{u}_i^n, \mathbf{u}_j^n, \mathbf{u}_i^*, \mathbf{u}_j^*) &= \beta \left(U_{i \rightarrow ij}^n + \frac{\mathbf{U}_i^h \big|_{ij}^* - \mathbf{U}_i^h \big|_{ij}^n + \mathbf{U}_j^h \big|_{ij}^* - \mathbf{U}_j^h \big|_{ij}^n}{2} \right) \\ &\quad + (1 - \beta) \left(\frac{\mathbf{U}_i^h \big|_{ij}^* + \mathbf{U}_j^h \big|_{ij}^*}{2} \right). \end{aligned} \quad (53)$$

Eq. (53) considers the temporal variation in $U_{i \rightarrow ij}$, thereby linking the velocity and pressure in time. Here, the parameter $\beta \in [0, 1]$ is introduced to avoid the inconsistent coupling between $U_{i \rightarrow ij}$ and the nodal velocities \mathbf{u}_i and \mathbf{u}_j . This parameter is set to $\beta = 0.99$ in this study.

3 Numerical tests

3.1 Linear acoustics

Our first investigation was validating the influence of the staggered arrangements of the velocity and pressure variables in the meshfree framework. The 2D linear acoustics problem with velocity and pressure variables was solved in the square domain $[0, L] \times [0, L]$. Parameters were set to $L = 1$, $\rho = 1050$, and $c = 1000$. The domain was discretized using $N \times N$ uniformly distributed DPs, and the calculations were performed at $N = 17, 33, 65, 129$, and 257 . The DP spacing l_0 (the background mesh width) can be written as $l_0 = L/(N - 1)$. The time interval was set to $\Delta t = 5 \times 10^{-8}$, so the Courant number corresponding to the acoustic speed was equal to $c\Delta t/l_0 = 1.28 \times 10^{-2}$ at $N = 257$. The calculation was executed until $t = 3 \times 10^{-4}$. The initial velocity field was set to zero, and the initial pressure field was given as

$$p(\mathbf{x}, 0) = \begin{cases} \frac{1}{2} \left(1 + \cos \left(\frac{\pi \|\mathbf{x} - \mathbf{x}_0\|}{R} \right) \right), & \text{if } \|\mathbf{x} - \mathbf{x}_0\| < R, \\ 0, & \text{otherwise.} \end{cases} \quad (54)$$

The parameters were set to $R = L/10$ and $\mathbf{x}_0 = (L/2, L/2)^\top$.

Fig. 5 shows the snapshots of pressure distributions calculated using the proposed staggered method with $N = 129$ at five time instants. These confirm that the pressure propagates axisymmetrically in a spatiotemporally smooth manner. Fig. 6 shows comparisons of the pressure distributions along the x -axis centerline in the range $[L/2, L]$ with the high-resolution reference solution obtained using the finite-difference time-domain (FDTD) method with $N = 2048$. Fig. 6 indicates that numerical solutions obtained using the proposed staggered method are closer to the high-resolution FDTD reference solution than those obtained via the conventional collocated method.

Fig. 7 shows (a) a snapshot of the pressure field in a system with a cylindrical obstacle ($N = 129$, $\Delta t = 10^{-7}$) at $t = 3 \times 10^{-4}$ obtained using the proposed staggered method, (b) one obtained via the conventional collocated method, and (c) the pressure distributions along the x -axis centerline. Here, a cylindrical obstacle was modeled using the momentum equation [Eq. (26)] with an additional damping term proportional to the velocity:

$$\rho \frac{\partial \mathbf{u}}{\partial t} = -\nabla p - \alpha_{\text{damp}} \rho \mathbf{u}, \quad (55)$$

where α_{damp} denotes the damping coefficient, which was defined using a constant α_0 as

$$\alpha_{\text{damp}}(\mathbf{x}) = \begin{cases} \frac{\alpha_0}{2} \left(1 + \cos \left(\frac{\pi \|\mathbf{x} - \mathbf{x}_{\text{c,damp}}\|}{R_{\text{damp}}} \right) \right), & \text{if } \|\mathbf{x} - \mathbf{x}_{\text{c,damp}}\| < R_{\text{damp}}, \\ 0, & \text{otherwise.} \end{cases} \quad (56)$$

In this study, the parameters were set to $\alpha_0 = 10^7$, $R_{\text{damp}} = L/20$, and $\mathbf{x}_{\text{c,damp}} = (5L/8, L/2)^\top$. According to Fig. 7, the proposed staggered method represents the pressure field without unphysical numerical oscillations. In contrast, the conventional collocated method yields unphysical checkerboard patterns in the vicinity of the cylindrical obstacle (b), and the pressure distribution is no longer represented appropriately because the large numerical oscillations are sufficient to obscure the physical characteristics of the phenomenon (c). These results confirm the effectiveness of the staggered arrangement of velocity and pressure variables in the meshfree framework.

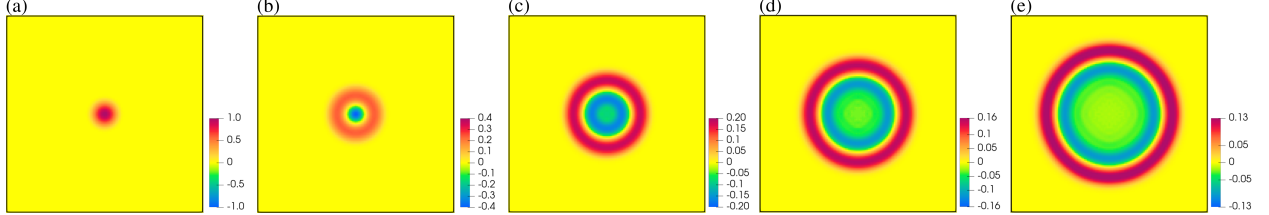


Figure 5: Snapshots of the pressure field for $N = 129$ at five times: (a) $t = 0$, (b) $t = 7.5 \times 10^{-5}$, (c) $t = 1.5 \times 10^{-4}$, (d) $t = 2.25 \times 10^{-4}$, and (e) $t = 3 \times 10^{-4}$, calculated using the staggered-variable arrangement.

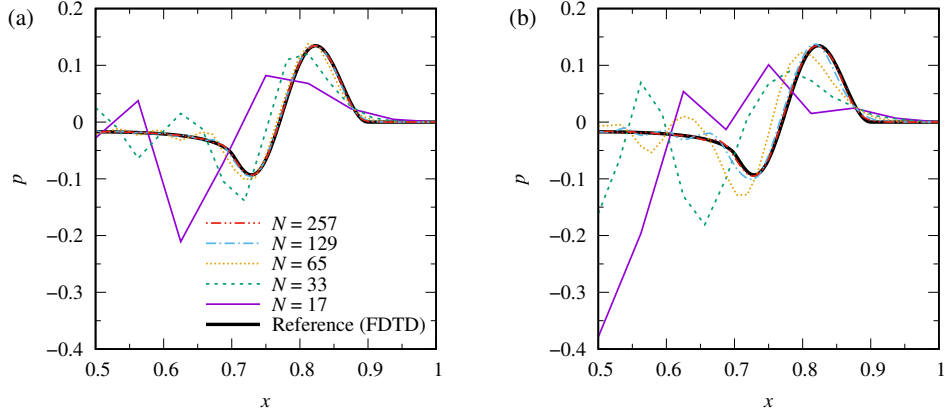


Figure 6: Comparisons of the pressure p along the x -axis for $x \in [L/2, L]$ using the MCD methods with the (a) staggered arrangement and (b) collocated arrangement. The black solid curves indicate the reference solution calculated with the FDTD method. The purple solid, green dashed, yellow dotted, blue dash-dot, and red dash-dot-dot curves correspond to resolutions $N = 17, 33, 65, 129$, and 257 , respectively.

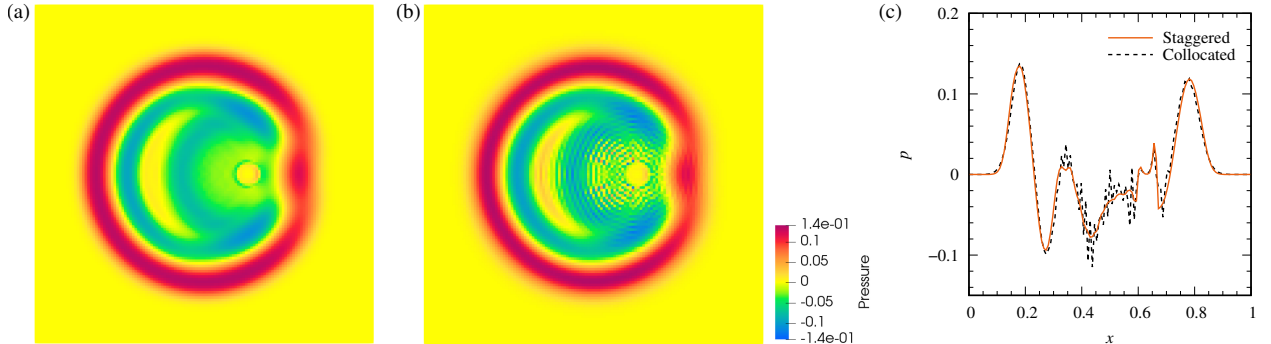


Figure 7: Snapshots of pressure fields ($N = 129$) at $t = 3 \times 10^{-4}$ in the presence of an obstacle, calculated using (a) the staggered-variable arrangement and (b) collocated arrangement. (c) Comparison of the pressure distributions along the x -axis, where the orange solid and black dashed lines correspond to the staggered and collocated arrangements, respectively.

3.2 Flow around a stationary cylinder

We calculated incompressible flows around a stationary cylinder of diameter D (Fig. 8) and investigated the effectiveness of the proposed velocity–pressure coupling strategy for incompressible Navier–Stokes equations. In this study, the cylinder diameter was set to $D = 1$, and the width and length of the channel were set to $H = 4D$ and $L = 8D$, respectively. The center of the cylinder was at the origin of the coordinate system, and the offset distance of the cylinder center from the inlet was set to $L_c = 2D$. The no-slip condition was imposed on the cylinder wall ($\mathbf{u} = \mathbf{0}$). Furthermore, the left-side channel boundary was subjected to the inlet condition ($\mathbf{u} = (U, 0)^\top$), and the right side was subjected to the outlet condition ($-p\mathbf{n} + \eta\partial\mathbf{u}/\partial n = \mathbf{0}$). To eliminate the influence of boundaries other than the cylinder wall, the side walls of the channel were subjected to periodic boundary conditions. The parameters were set to $U = 1$, $\rho = 1$, and $\eta = 5 \times 10^{-2}$, yielding Reynolds number $Re = \rho U D / \eta = 200$. The background mesh width was set to $l_0 = 1/32$, and the rectangular channel was represented using 257×130 DPs. The reference time interval was set to $\Delta t^* = 5 \times 10^{-3}$, so the Courant number was equal to $U\Delta t^*/l_0 = 0.16$. In this study, the time intervals $\Delta t = \Delta t^*$ and $0.01\Delta t^*$ were employed to investigate the influence of time resolution on the flow field. The linear system of the pressure Poisson equation was solved using the Bi-CGSTAB method [48]. The iterations were stopped when the relative L_2 residual norm of the linear system fell below the convergence criterion $\varepsilon_{\text{crit}}$, which was set to $\varepsilon_{\text{crit}} = 10^{-5}$ in this study.

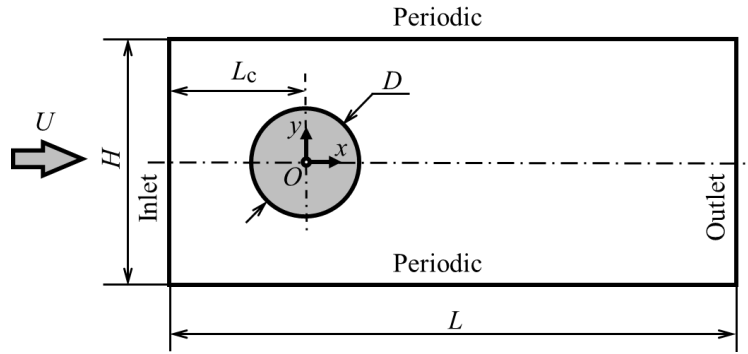


Figure 8: Illustration of the fluid flow problem around a cylinder.

Fig. 9 shows the pressure and vorticity fields obtained using (a) the proposed staggered method with the TEC parameter $\beta = 0.99$, (b) the staggered method with $\beta = 0$, and (c) the conventional collocated method. Fig. 10 shows velocity divergence fields. According to Fig. 9, the calculated flow fields are spatiotemporally smooth, and vortices are periodically shed in the cylinder wake at the coarse time resolution of $\Delta t = \Delta t^*$. Fig. 10 indicates that, in the proposed staggered method (a, b), the velocity divergence has an order of magnitude consistent with that of the convergence criterion of the pressure Poisson equation, regardless of whether the TEC is enabled. These results are attributed to the spatial discretization scheme based on the MLS reconstruction with radial components, which guarantees algebraic consistency between the discrete gradient and divergence operators. In contrast, the result of the conventional collocated method [Fig. 10 (c)], which uses ordinary MLS for spatial discretization, yields a velocity divergence field with a much larger order of magnitude than that expected from the convergence criterion of the pressure Poisson equation. These results show that the proposed staggered method achieves incompressible fluid flow at the discrete level in the meshfree framework.

Fig. 11 shows the snapshots of pressure fields around the cylinder at $t = 2$ and 100 for $\Delta t = 0.01\Delta t^*$ obtained using (a) the proposed staggered method with $\beta = 0.99$, (b) the proposed staggered method with $\beta = 0$, and (c) the conventional collocated method. Fig. 12 shows the pressure fields, where a cylindrical obstacle is represented by a uniform DP arrangement using the momentum equation [Eq. (35)] with a damping term proportional to the velocity:

$$\frac{\partial(\rho\mathbf{u})}{\partial t} + \nabla \cdot (\rho\mathbf{u}\mathbf{u}) = -\nabla p + \nabla \cdot \boldsymbol{\tau} - \alpha_{\text{damp}}\rho\mathbf{u}, \quad (57)$$

where α_{damp} is also calculated from Eq. (56). The parameters were set to $\alpha_0 = 10^4$, $R_{\text{damp}} = D/2$, and $\mathbf{x}_{c,\text{damp}} = (0, 0)^\top$. This obstacle treatment enables us to investigate the influence of the wall boundary on the fluid flow while excluding the nonuniform DP arrangement along the cylinder. According to Figs. 11 and 12, the proposed staggered method with $\beta = 0.99$ obtained a spatiotemporally smooth pressure field. In contrast, the pressure showed checkerboard instability in the vicinity of the cylinder at $t = 2$ in the proposed staggered method with $\beta = 0$ (b) and the conventional collocated method (c), regardless of whether the DP arrangement was uniform. Meanwhile, the flow calculation did not fail even if the conventional collocated method was used for an empty channel. Thus, the presence of the obstacle itself causes the checkerboard instability in the pressure. These results confirm that the velocity and pressure are temporally linked by the TEC formula and are consistently coupled. Although the proposed method with $\beta = 0$ stably reproduced periodic vortex shedding despite checkerboard pressure oscillations near the cylinder, the conventional collocated method failed shortly after $t = 2$. We attribute the successful calculation in the staggered method to the spatial discretization scheme, which satisfies the algebraic consistency of the discrete gradient and divergence operator, resulting in numerical incompressibility at the discrete level.

These results confirm that introducing a staggered arrangement of velocity and pressure variables together with a consistent velocity–pressure coupling with TEC in the meshfree framework enables stable calculation of the temporal evolution of incompressible flows.

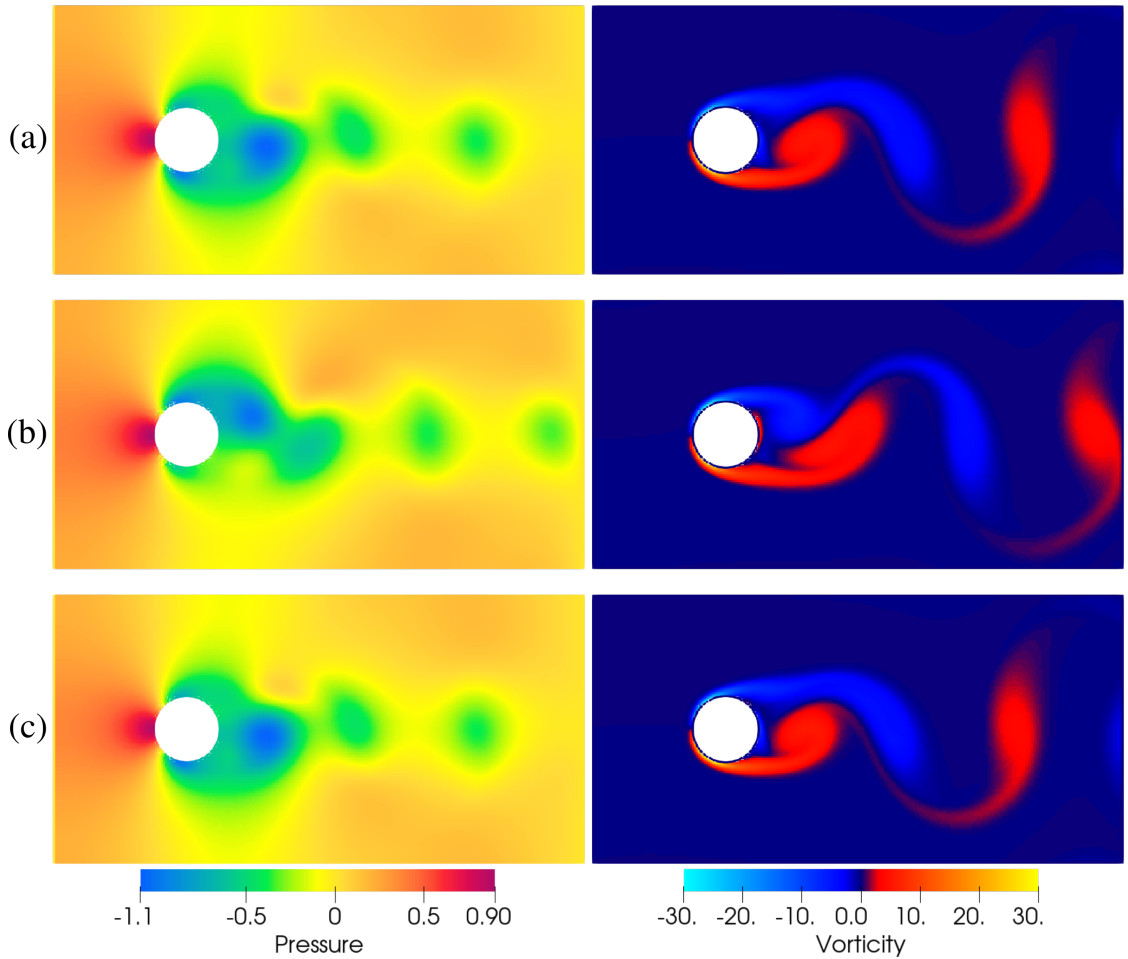


Figure 9: Snapshots at $t = 100$ of pressure and vorticity fields around a cylinder at $Re = 200$ for $\Delta t = \Delta t^*$. (a) Proposed staggered arrangement with $\beta = 0.99$, (b) staggered arrangement with $\beta = 0$, and (c) conventional collocated arrangement.

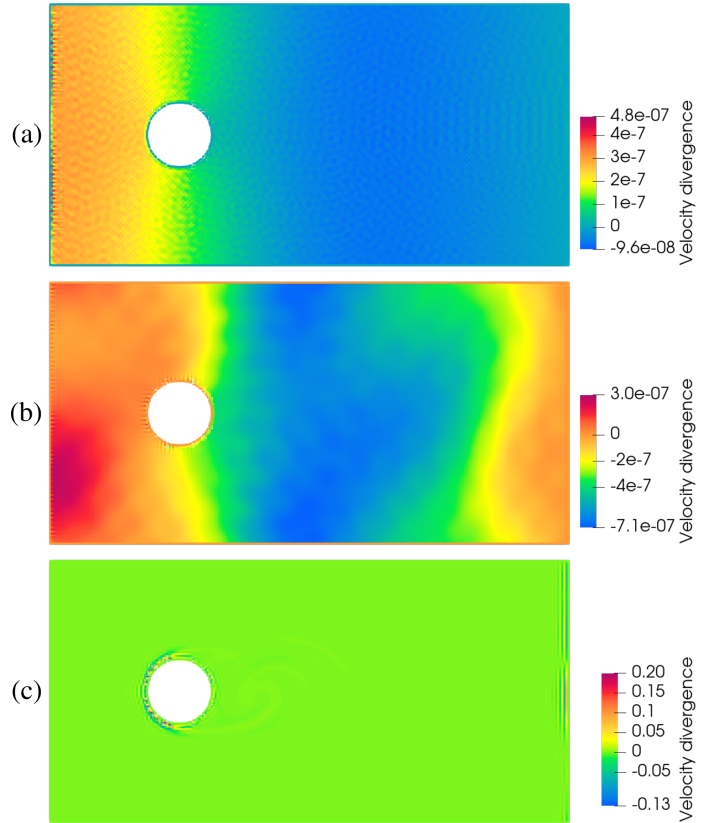


Figure 10: Snapshots at $t = 100$ of velocity divergence around a cylinder at $Re = 200$ for $\Delta t = \Delta t^*$. (a) Proposed staggered arrangement with $\beta = 0.99$, (b) staggered arrangement with $\beta = 0$, and (c) conventional collocated arrangement.

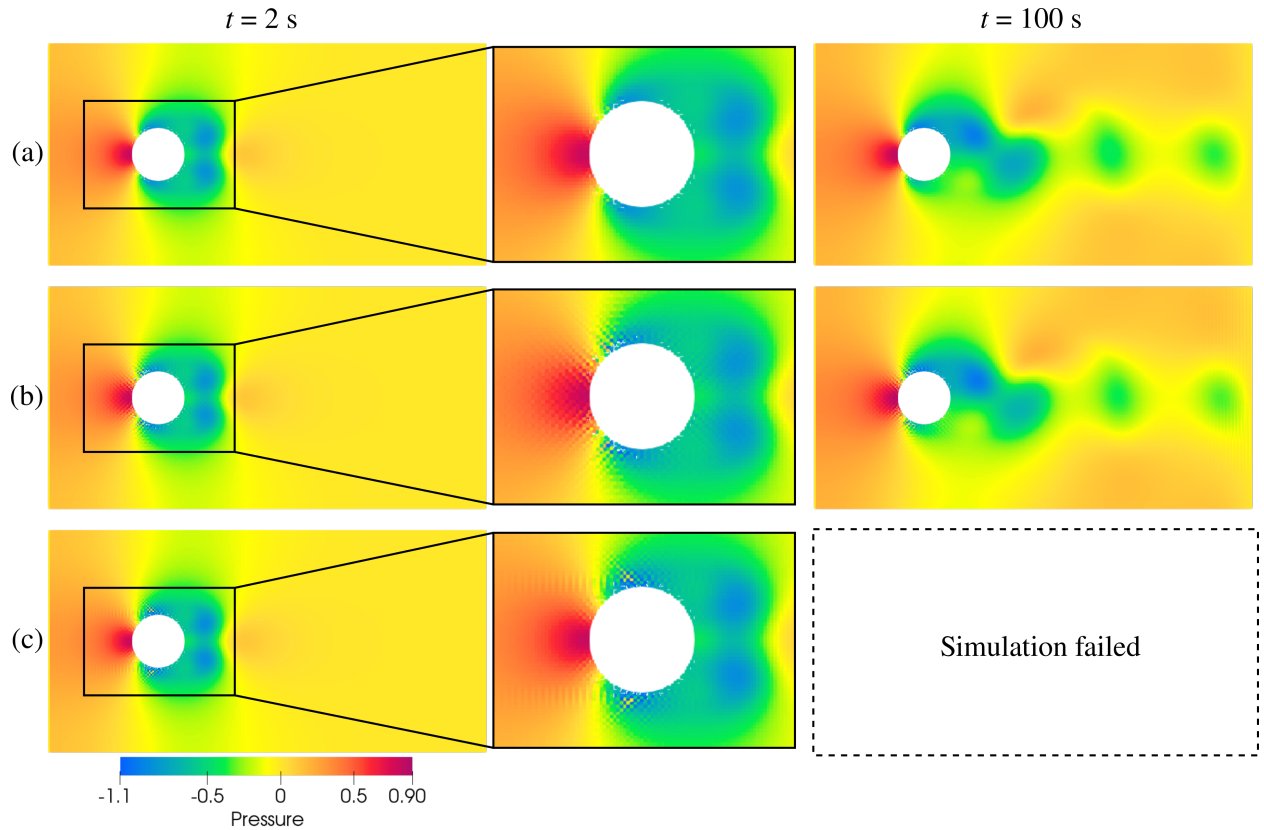


Figure 11: Pressure distribution around a circular cylinder at $Re = 200$ for $\Delta t = 0.01\Delta t^*$. (a) Staggered arrangement with TEC ($\beta = 0.99$), (b) staggered arrangement without TEC ($\beta = 0$), and (c) conventional collocated arrangement.

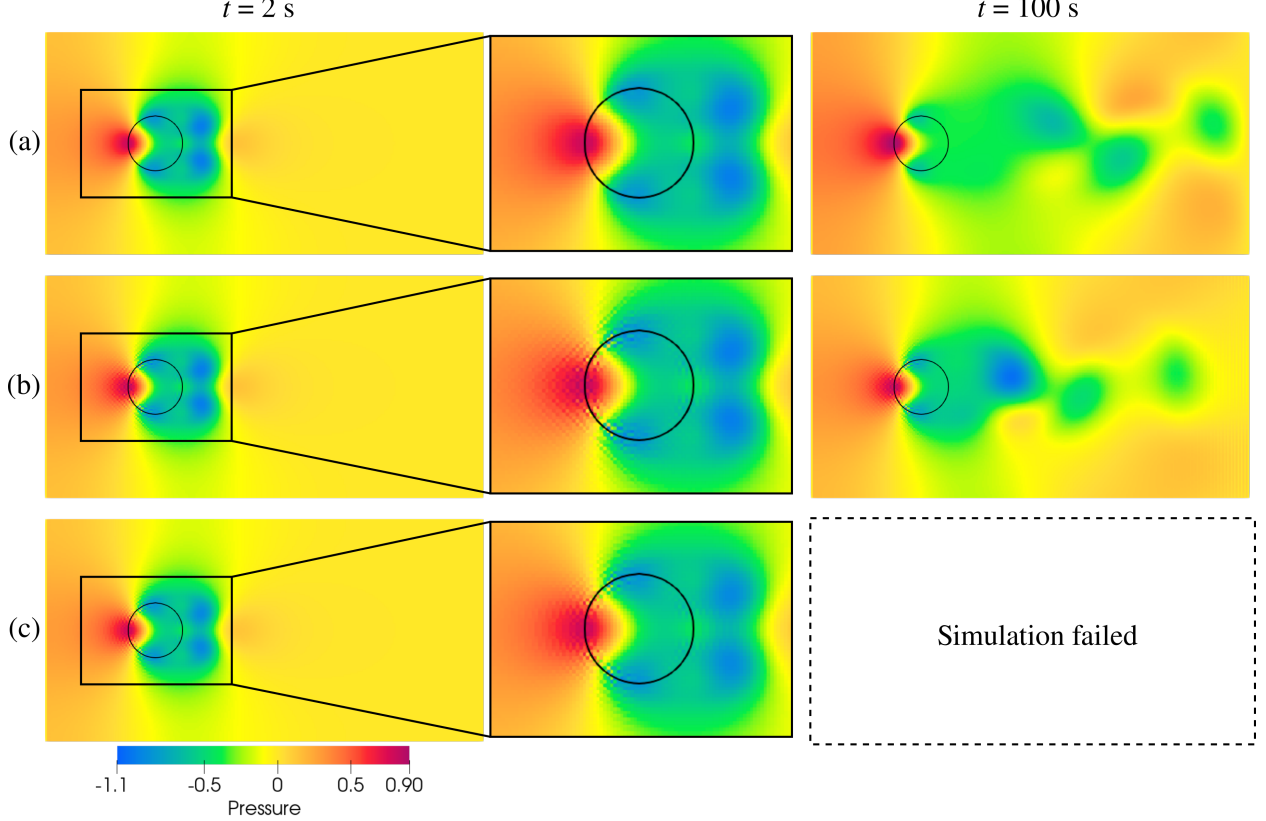


Figure 12: Pressure distribution around a circular obstacle ($Re = 200$, $\Delta t = 0.01\Delta t^*$) represented by a damping term proportional to velocity. The black solid curve indicates the nominal position of the obstacle boundary. (a) Staggered arrangement with TEC ($\beta = 0.99$), (b) staggered arrangement without TEC ($\beta = 0$), and (c) conventional collocated arrangement.

3.3 Periodic Taylor–Green vortex

In this section, we investigate the spatial convergence accuracy by solving the Taylor–Green vortex problem in the square domain $[-L, L] \times [-L, L]$. Periodic boundary conditions are imposed on all boundaries. The exact solutions of the u and v components of velocities and pressure at t are

$$u_e(\mathbf{x}, t) = U \exp\left(-\frac{2\pi^2\eta t}{\rho L^2}\right) \sin\left(\frac{\pi x}{L}\right) \cos\left(\frac{\pi y}{L}\right), \quad (58)$$

$$v_e(\mathbf{x}, t) = -U \exp\left(-\frac{2\pi^2\eta t}{\rho L^2}\right) \cos\left(\frac{\pi x}{L}\right) \sin\left(\frac{\pi y}{L}\right), \quad (59)$$

$$p_e(\mathbf{x}, t) = \frac{\rho U^2}{4} \exp\left(-\frac{4\pi^2\eta t}{\rho L^2}\right) \left[\cos\left(\frac{\pi x}{L}\right) + \cos\left(\frac{\pi y}{L}\right) \right], \quad (60)$$

where U denotes the reference velocity magnitude. The initial velocity field is given by the exact solution at $t = 0$. In this study, we set the parameters to $U = 1$, $L = 1$, $\rho = 1$, and $\eta = 0.01$. The Reynolds number, defined as $Re = \rho U L / \eta$, was set to 100. The DP spacing (or width of a background mesh element defined as $l_0 = 2L/N$, where N is the number of DPs in each direction) was doubly increased from $N = 8$ to 1024. The time step was set to $\Delta t = 1 \times 10^{-5}$, which was independent of the spatial resolution, so the diffusion number was $C_{\text{diff}} = \eta \Delta t / (\rho l_0^2) = 0.0262$ at $N = 1024$. The linear system of the pressure Poisson equation was solved using the Bi-CGSTAB method with the Lagrangian multiplier to constrain the pressure field to have zero mean over the domain. The iteration was terminated when the absolute L_2 residual norm fell below the

convergence criterion $\varepsilon_{\text{crit}} = 10^{-7}$. We calculated the temporal change in fluid flow for the uniform DP arrangement [Fig. 13(a)] and the randomized DP arrangement [Fig. 13(b)]. The random DP arrangement was generated by shifting each DP using random displacement vector $\delta\mathbf{x} = (\delta x, \delta y)^\top$ from the center of the background mesh element, where δx and δy are independently and identically distributed according to the uniform distribution $\mathcal{U}(-\alpha_{\text{rdm}}l_0/2, \alpha_{\text{rdm}}l_0/2)$. The amplification coefficient α_{rdm} was set to 0.5.

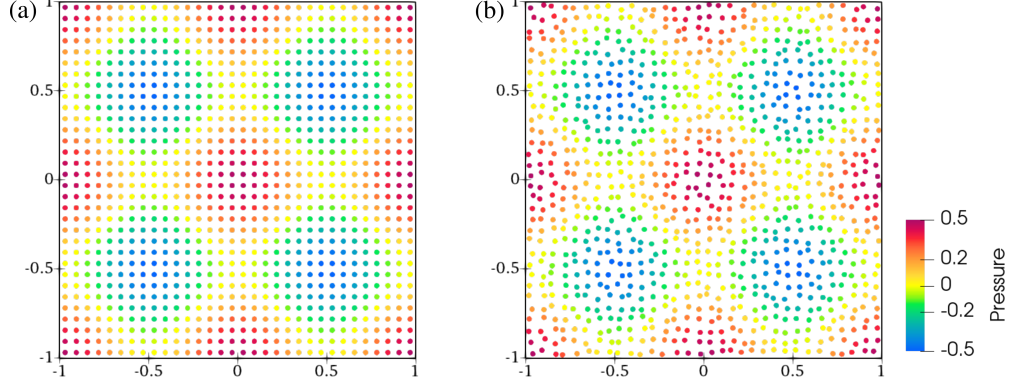


Figure 13: Computational domain of the Taylor–Green vortex ($N = 32$) for (a) uniform DP arrangement and (b) randomized DP arrangement. Periodic boundary conditions are imposed on all boundaries. The color map indicates the initial pressure field.

The numerical errors in L_1 , L_2 , and L_∞ norms are defined as

$$L_1 = \frac{1}{N} \sum_{\mathbf{x}_i \in \Omega} |\phi(\mathbf{x}_i) - \phi_e(\mathbf{x}_i)|, \quad (61)$$

$$L_2 = \sqrt{\frac{1}{N} \sum_{\mathbf{x}_i \in \Omega} |\phi(\mathbf{x}_i) - \phi_e(\mathbf{x}_i)|^2}, \quad (62)$$

$$L_\infty = \max_{\mathbf{x}_i \in \Omega} |\phi(\mathbf{x}_i) - \phi_e(\mathbf{x}_i)|, \quad (63)$$

where $\phi \in \{u, v, p\}$ is the numerical solution calculated using the proposed method, and ϕ_e is the corresponding exact solution (u_e, v_e, p_e) .

Figs. 14 and 15 show spatial convergences of L_1 , L_2 , and L_∞ error norms at $t = 0.1$ for (a) u , (b) v , and (c) p for the uniform and randomized DP arrangements, respectively. The proposed second-order MLS reconstruction shows approximately second-order spatial convergence accuracy for velocity and pressure in both the uniform and random DP arrangements.

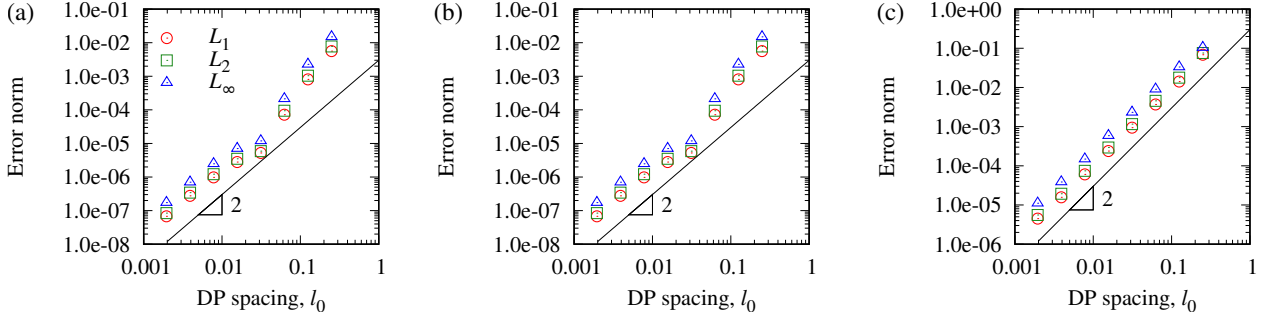


Figure 14: Spatial convergence of L_1 , L_2 , and L_∞ error norms at $t = 0.1$ for (a) the x component of velocity, (b) the y component of velocity, and (c) the pressure for a uniform DP arrangement.

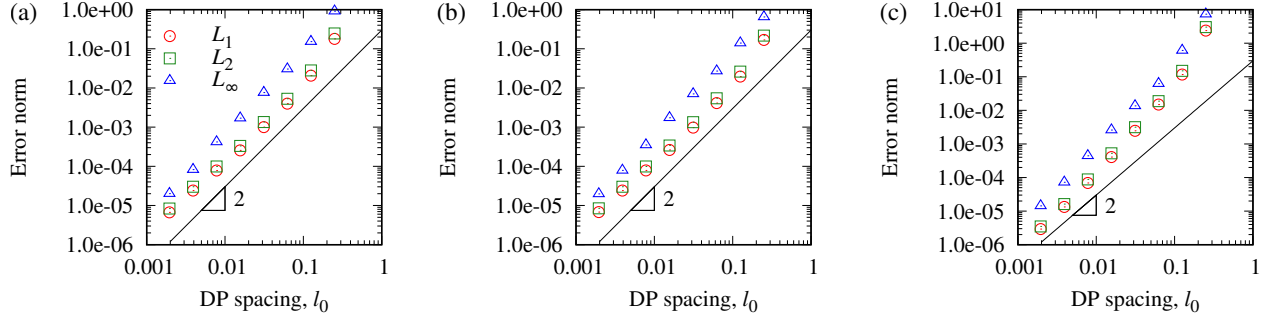


Figure 15: Same as Fig. 14, but for the randomized DP arrangement.

3.4 Lid-driven cavity flow

We calculated the two-dimensional lid-driven cavity flow to demonstrate the applicability of the proposed method over a wide range of Reynolds numbers. This problem is a classical benchmark for incompressible Navier–Stokes solvers and has been validated by many researchers [49, 50, 51, 52]. In this study, the flow was calculated in a $[-L/2, L/2] \times [-L/2, L/2]$ square domain, where L is the characteristic length set to $L = 1$. The boundary condition $\mathbf{u} = (U, 0)^\top$ for velocity was imposed on the upper wall, which drives the flow. The quantity U is the characteristic flow speed, which was set to $U = 1$. The other three walls were subject to the no-slip boundary condition ($\mathbf{u} = \mathbf{0}$). We set the fluid density to $\rho = 1$, and set the viscosity η by setting the Reynolds number $Re = \rho U L / \eta$ as $Re = 100, 1000$, and 5000 . The square domain was discretized using $N \times N$ DPs. The flows at $Re = 100$ and 1000 were calculated with $N = 33, 65$, and 129 , while the flows at $Re = 5000$ were calculated with $N = 65, 129$, and 257 . The time interval was set such that the Courant number was equal to 0.128 . The linear system of the pressure Poisson equation was solved using Bi-CGSTAB with the Lagrangian multiplier constraint that the mean pressure over the domain was 0 . Bi-CGSTAB iterations were stopped when the relative L_2 residual norm was less than the convergence criterion $\varepsilon_{\text{crit}} = 10^{-7}$. The flow was simulated until the maximum temporal variation rate of each velocity component was less than 10^{-3} .

Fig. 16 shows the streamlines of the cavity flows at (a) $Re = 100$, (b) $Re = 1000$, and (c) $Re = 5000$ at the final timestep. In these snapshots, the primary vortex becomes larger and shifts toward the center of the square domain as the Reynolds number increases. Secondary vortices developed in the lower left and right corners. At $Re = 5000$, an additional secondary vortex appeared in the upper left corner, and a tertiary vortex formed in the lower right corner. These tendencies are in good agreement with previously reported numerical results [49, 50, 52]. Fig. 17 shows the velocity profiles along the horizontal and vertical centerlines of the square domain. The proposed staggered approach obtains a more accurate solution than that of the conventional collocated formulation as the Reynolds number increases. At $Re = 5000$, the results of the staggered approach at $N = 129$ [Fig. 17(g, h)] are closer to the reference data of Ghia *et al.* [49] than those of the $N = 257$ solution of the collocated method [Fig. 17(i)]. These convincingly show that the consistency of the discrete gradient and divergence operators (in satisfying incompressibility at the discrete level) is important for simulating the higher-Reynolds-number flow in the projection-based meshfree framework. Moreover, comparing $\beta = 0.99$ and $\beta = 0$ in the staggered method indicates that the TEC formula provides more accurate flow characteristics for all Reynolds numbers.

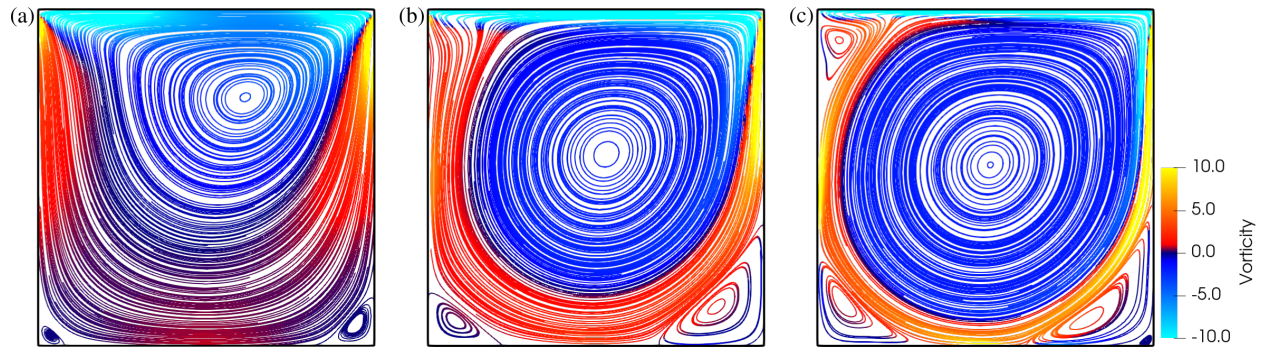


Figure 16: Streamline visualizations of the lid-driven cavity flow calculated using the proposed staggered MCD method at (a) $Re = 100$ with 129×129 (snapshot at $t = 9.322$), (b) $Re = 1000$ with 129×129 ($t = 34.229$), and (c) $Re = 5000$ with 257×257 ($t = 176.6615$). The vorticity field is visualized with contours limited to the range $[-10, 10]$ to highlight the vortex structures in the cavity interior, while higher magnitudes near the walls are omitted.

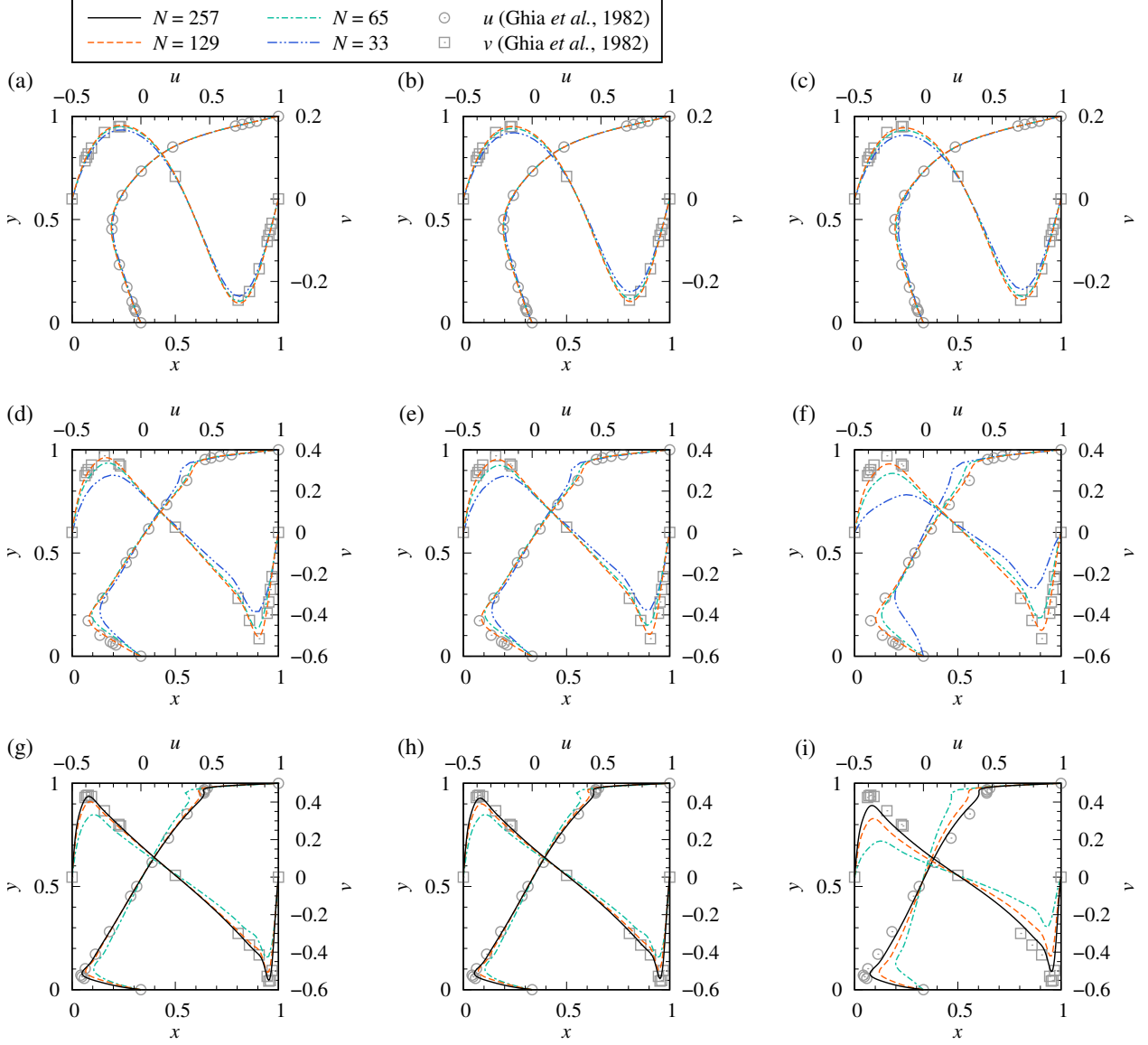


Figure 17: Centerline velocity profiles of the lid-driven cavity flow compared with the reference data of Ghia *et al.* [49] for (a–c) $Re = 100$, (d–f) $Re = 1000$, and (g–i) $Re = 5000$. Panels (a, d, g) show the proposed staggered method with $\beta_{TEC} = 0.99$, (b, e, h) use $\beta_{TEC} = 0$, and (c, f, i) show the previous collocated MCD method. Black solid, orange dashed, green dash-dot, and blue dash-dot-dot curves represent $N = 257, 129, 65$, and 33 , respectively. Gray circles and squares are the reference data for u and v , respectively.

3.5 Flow around a periodically oscillating cylinder

As a final test case, we calculated the flow around a periodically oscillating cylinder of diameter D . Although this problem has been used as a benchmark to validate a flow solver in moving boundary problems [53, 54, 55, 56, 20], in this study, the flow was calculated in a coordinate system $\tilde{\mathbf{x}}$ fixed to the moving cylinder to eliminate the effect of updating the DP arrangement around the moving cylinder and to validate the flow solver itself. According to the Galilean transformation, the moving coordinate system $\tilde{\mathbf{x}}$ was defined as $\tilde{\mathbf{x}} = \mathbf{x} - \mathbf{x}_{cyl}$, where $\mathbf{x}_{cyl} = (x_{cyl}, y_{cyl})^\top$ is the cylinder center. In the coordinate system fixed to the moving

cylinder, the momentum equation can be written as

$$\frac{\partial(\rho\mathbf{u})}{\partial t} + \nabla \cdot (\rho\mathbf{u}\mathbf{u}) = -\nabla p + \nabla \cdot \boldsymbol{\tau} - \rho\ddot{\mathbf{x}}_{\text{cyl}}. \quad (64)$$

In this study, the cylinder motion was given as $x_{\text{cyl}} = -A \sin(2\pi ft)$, $y_{\text{cyl}} = 0$, where $A = U/2\pi f$ denotes the amplitude coefficient of the cylinder motion, and U and f are the characteristic velocity magnitude of the cylinder and the frequency. The Reynolds number Re and Keulegan–Carpenter number KC of the flow were defined as $Re = \rho UD/\eta$ and $KC = U/fD$, and were set to $Re = 100$ and $KC = 5$. Parameters were set to $D = 1$, $f = 1$, $U = 5$, $\rho = 1$, and $\eta = 5 \times 10^{-2}$. The side length of the computational domain was set to $L = 20D$. The width of the background mesh was set to $l_0 = 2.5 \times 10^{-2}$, and the time interval to $\Delta t = 1/900$. The no-slip boundary conditions were imposed on all the walls. We calculated the linear system of the pressure Poisson equation using Bi-CGSTAB with the Lagrangian multiplier constraint that the mean pressure is zero. In this problem, the iteration for solving pressure was terminated when the relative L_2 error norm of Bi-CGSTAB fell below the convergence criterion $\varepsilon_{\text{crit}} = 10^{-5}$. The TEC parameter β was set to 0.99.

Fig. 18 shows the contours of the pressure and vorticity around the cylinder at four phase angles calculated with the proposed method. The results show the asymmetric pressure distribution between the upstream and downstream sides of the cylinder caused by inertial effects, as well as the periodic vortex shedding in the wake behind the cylinder. Both the pressure and vorticity are in good agreement with the well-validated numerical solution of Dütsch *et al.* using a fixed body-fitted mesh [53]. Fig. 19 shows the comparisons of the x and y components of the velocity profiles with published experimental results [53] at four cross-sections and three phase angles. These graphs show that the velocity calculated with the proposed method is in good agreement with both the experimental and numerical results. Fig. 20 shows the temporal change in the drag coefficient C_D and its components (pressure and viscosity), and the results are in good agreement with the reference numerical solutions [53, 54].

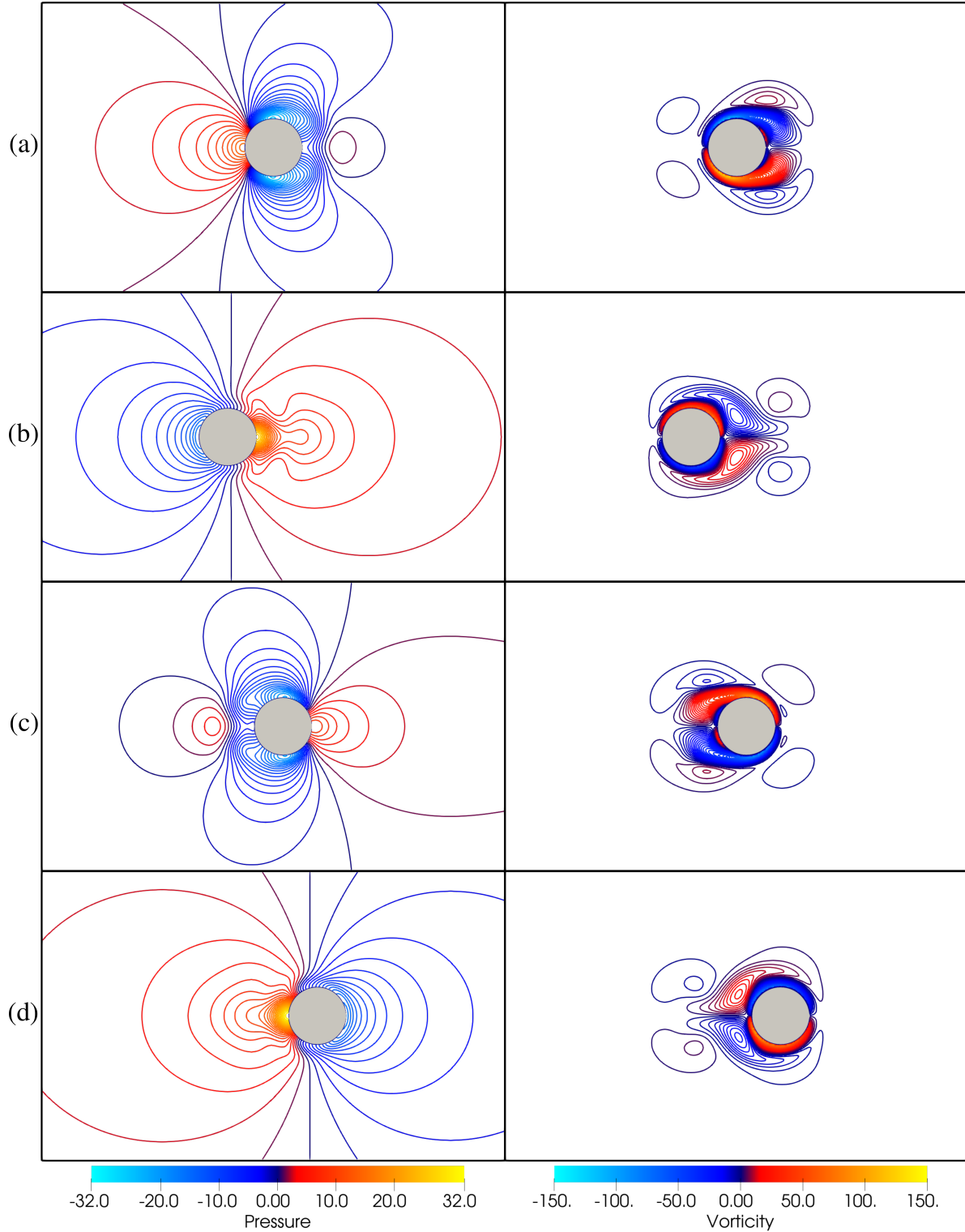


Figure 18: Numerical results for the pressure (left) and vorticity (right) isolines around an oscillating cylinder. The phase angles of the cylinder position are (a) 0° , (b) 96° , (c) 192° , and (d) 288° . The pressure contour levels are -32 to 32 in increments of 1.28 , and the vorticity contour levels are -150 to 150 in increments of 2.4 .

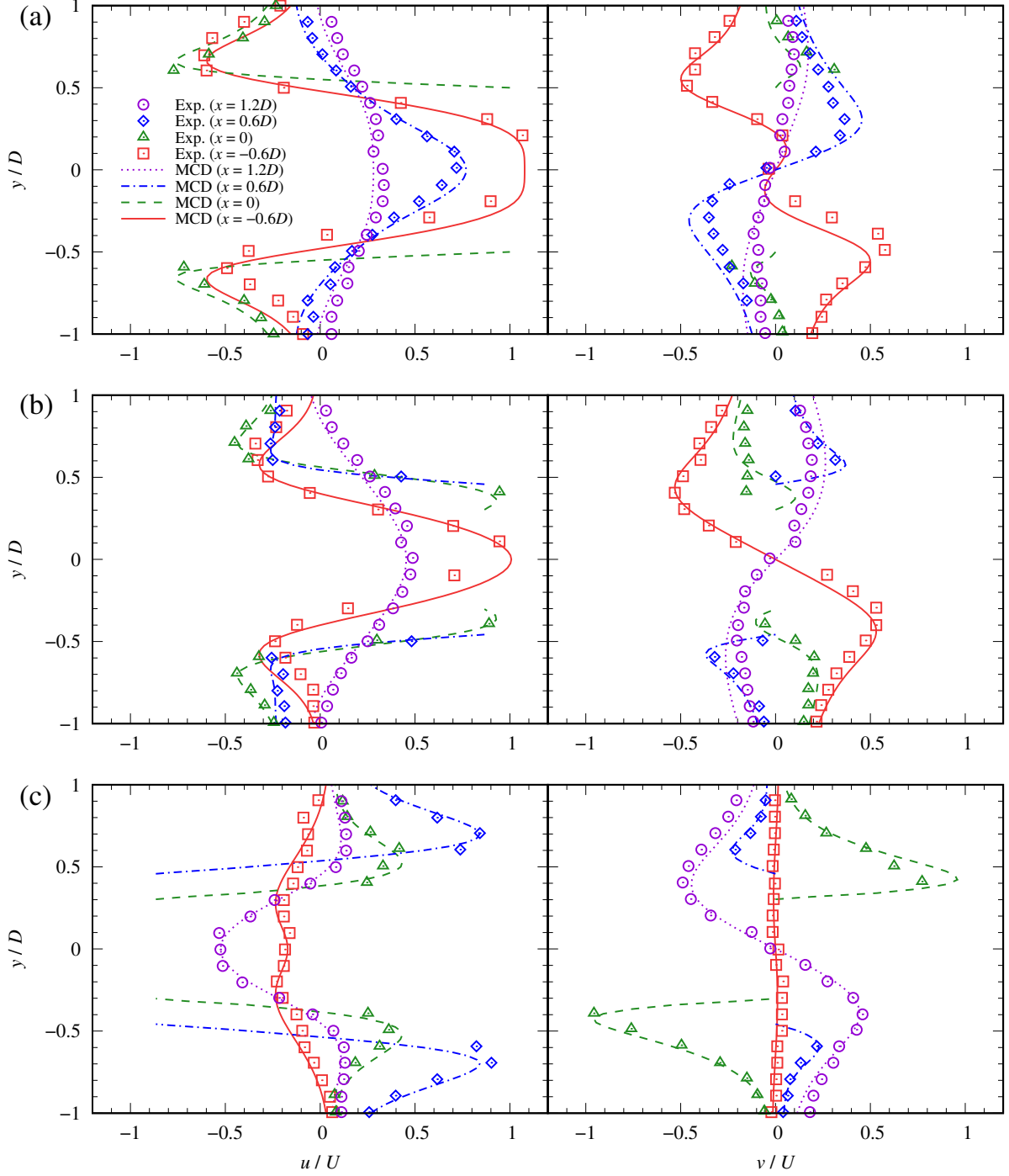


Figure 19: Comparisons of x and y components of velocities for four cross-sections: $x = -0.6D$ (red curve/squares), $x = 0$ (green dashed curve/triangles), $x = 0.6D$ (blue dash-dotted curve/diamonds), and $x = 1.2D$ (purple dotted curve/circles). The phase angles of the cylinder position are (a) 180° , (b) 210° , and (c) 330° . Experimental results are taken from [53].

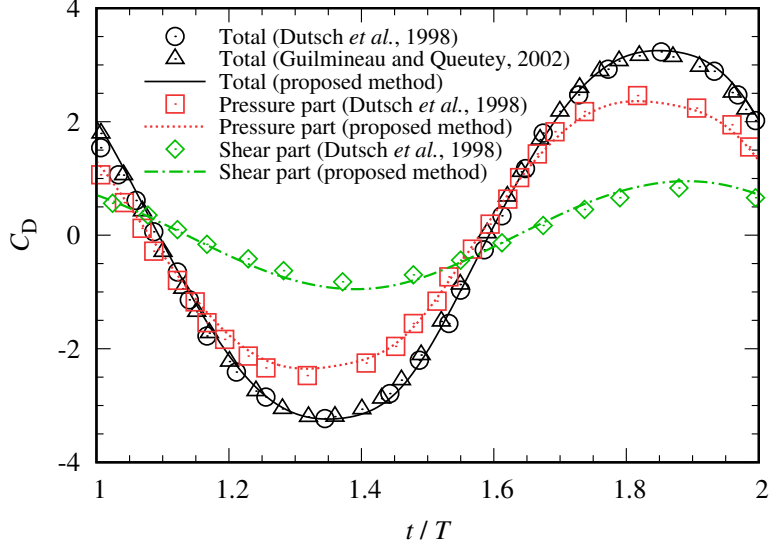


Figure 20: Comparison of the time variation in the drag force coefficient and its components. $T = 1/f$ is the period of cylinder motion. The circles/triangles/squares/diamonds indicate previous results [53, 54].

4 Conclusion

This study proposed a least-squares strong-form meshless method for the incompressible Navier–Stokes equations. The proposed method adopts MLS reconstruction with radial components defined at staggered points (i.e., midpoints between each DP and its neighbors) for the spatial discretization. The proposed method consistently evaluates the discrete gradient and divergence operators, thereby guaranteeing incompressibility at the numerical level, which has been inherently challenging in strong-form meshfree frameworks employing projection-based velocity–pressure coupling. Moreover, in the proposed method, the radial velocity components with a nonlinear advection term are evaluated on staggered points using the TEC formula, which links the temporal variation between the velocity and pressure. This achieves a consistent velocity–pressure coupling and suppresses the checkerboard pressure instability commonly observed in collocated methods. Several numerical tests indicate that the proposed method achieves approximately second-order spatial convergence accuracy for both velocity and pressure, as expected from the formulation, and reproduces incompressible flows more accurately than the conventional collocated method over a wide range of Reynolds numbers. The formulation is implemented within the MCD framework using compact 3×3 stencils and demonstrates efficient and accurate calculations. These results demonstrate that the proposed method offers a promising direction for further developing stable, accurate, and high-fidelity incompressible flow solvers in strong-form meshfree frameworks.

Acknowledgments

The authors thank Dr. Hiro Wakimura (Institute of Science Tokyo) for his constructive comments on the numerical scheme. This work was supported by JST SPRING Grant Number JPMJSP2156; JSPS KAKENHI Grant Numbers JP24KJ1851, JP22H00190, and JP24K02557; the MEXT Program for Promoting Researches on the Supercomputer Fugaku (Development of human digital twins for cerebral circulation using Fugaku, Grant Number JPMXP1020230118). This study used computational resources of the supercomputer Fugaku provided by the RIKEN Center for Computational Science (project IDs: hp230208, hp240220, hp250236, hp240080, hp240458, and hp250282). Some computations were also carried out using the supercomputer Flow at the Information Technology Center, Nagoya University. The work was partly supported by the Research Organization for Information Science & Technology (RIST) under the HPCI User Support Program. Mark

R. Kurban from Edanz (<https://www.jp.edanz.com/ac>) edited a draft of this paper.

Conflict of interest

The authors declare that they have no known competing financial interests or personal relationships that could have appeared to influence the work reported in this paper.

Author contributions

Takeharu Matsuda: Writing—original draft, Visualization, Validation, Software, Methodology, Investigation, Data curation, Conceptualization. **Satoshi Ii:** Writing—review & editing, Validation, Software, Methodology, Conceptualization.

Data availability

Data will be made available on request.

References

- [1] T. Belytschko, Y. Y. Lu, L. Gu, Element-free Galerkin methods, *Int. J. Numer. Methods Eng.* 37 (2) (1994) 229–256. [doi:10.1002/nme.1620370205](https://doi.org/10.1002/nme.1620370205).
- [2] X. Wang, J. Ouyang, J. Su, B. Yang, On the superiority of the mixed element free Galerkin method for solving the steady incompressible flow problems, *Eng. Anal. Bound. Elem.* 36 (11) (2012) 1618–1630. [doi:10.1016/j.enganabound.2012.05.006](https://doi.org/10.1016/j.enganabound.2012.05.006).
- [3] S. N. Atluri, T. Zhu, A new Meshless Local Petrov-Galerkin (MLPG) approach in computational mechanics, *Comput. Mech.* 22 (2) (1998) 117–127. [doi:10.1007/s004660050346](https://doi.org/10.1007/s004660050346).
- [4] M. Abbaszadeh, M. Dehghan, Direct meshless local Petrov–Galerkin (DMLPG) method for time-fractional fourth-order reaction–diffusion problem on complex domains, *Comput. Math. Appl.* 79 (3) (2020) 876–888. [doi:10.1016/j.camwa.2019.08.001](https://doi.org/10.1016/j.camwa.2019.08.001).
- [5] W. K. Liu, S. Jun, Y. F. Zhang, Reproducing kernel particle methods, *Int. J. Numer. Methods Fluids* 20 (8-9) (1995) 1081–1106. [doi:10.1002/fld.1650200824](https://doi.org/10.1002/fld.1650200824).
- [6] R. A. Gingold, J. J. Monaghan, Smoothed particle hydrodynamics: Theory and application to non-spherical stars, *Mon. Not. R. Astron. Soc.* 181 (3) (1977) 375–389. [doi:10.1093/mnras/181.3.375](https://doi.org/10.1093/mnras/181.3.375).
- [7] S. Koshizuka, Y. Oka, Moving-Particle Semi-Implicit Method for Fragmentation of Incompressible Fluid, *Nucl. Sci. Eng.* 123 (3) (1996) 421–434. [doi:10.13182/NSE96-A24205](https://doi.org/10.13182/NSE96-A24205).
- [8] E. Oñate, S. Idelsohn, O. C. Zienkiewicz, R. L. Taylor, C. Sacco, A stabilized finite point method for analysis of fluid mechanics problems, *Comput. Methods Appl. Mech. Eng.* 139 (1) (1996) 315–346. [doi:10.1016/S0045-7825\(96\)01088-2](https://doi.org/10.1016/S0045-7825(96)01088-2).
- [9] N. Perrone, R. Kao, A general finite difference method for arbitrary meshes, *Comput. Struct.* 5 (1) (1975) 45–57. [doi:10.1016/0045-7949\(75\)90018-8](https://doi.org/10.1016/0045-7949(75)90018-8).
- [10] T. Liszka, J. Orkisz, The finite difference method at arbitrary irregular grids and its application in applied mechanics, *Comput. Struct.* 11 (1) (1980) 83–95. [doi:10.1016/0045-7949\(80\)90149-2](https://doi.org/10.1016/0045-7949(80)90149-2).
- [11] J. J. Benito, F. Ureña, L. Gavete, Solving parabolic and hyperbolic equations by the generalized finite difference method, *J. Comput. Appl. Math.* 209 (2) (2007) 208–233. [doi:10.1016/j.cam.2006.10.090](https://doi.org/10.1016/j.cam.2006.10.090).

[12] F. U. Prieto, J. J. Benito Muñoz, L. G. Corvinos, Application of the generalized finite difference method to solve the advection–diffusion equation, *J. Comput. Appl. Math.* 235 (7) (2011) 1849–1855. [doi:10.1016/j.cam.2010.05.026](https://doi.org/10.1016/j.cam.2010.05.026).

[13] Z. Tang, H. Pan, Z. Fu, M. Chen, L. Ling, A least-squares generalized finite difference method for solving nonlinear reaction–diffusion systems, *Eng. Anal. Bound. Elem.* 179 (2025) 106351. [doi:10.1016/j.enganabound.2025.106351](https://doi.org/10.1016/j.enganabound.2025.106351).

[14] G. A. Dilts, Moving-least-squares-particle hydrodynamics—I. Consistency and stability, *Int. J. Numer. Methods Eng.* 44 (8) (1999) 1115–1155. [doi:10.1002/\(SICI\)1097-0207\(19990320\)44:8<1115::AID-NME547>3.0.CO;2-L](https://doi.org/10.1002/(SICI)1097-0207(19990320)44:8<1115::AID-NME547>3.0.CO;2-L).

[15] P. Suchde, J. Kuhnert, S. Tiwari, On meshfree GFDM solvers for the incompressible Navier–Stokes equations, *Comput. Fluids* 165 (2018) 1–12. [doi:10.1016/j.compfluid.2018.01.008](https://doi.org/10.1016/j.compfluid.2018.01.008).

[16] T. Tamai, S. Koshizuka, Least squares moving particle semi-implicit method, *Comput. Part. Mech.* 1 (3) (2014) 277–305. [doi:10.1007/s40571-014-0027-2](https://doi.org/10.1007/s40571-014-0027-2).

[17] T. Matsunaga, A. Södersten, K. Shibata, S. Koshizuka, Improved treatment of wall boundary conditions for a particle method with consistent spatial discretization, *Comput. Methods Appl. Mech. Eng.* 358 (2020) 112624. [doi:10.1016/j.cma.2019.112624](https://doi.org/10.1016/j.cma.2019.112624).

[18] Y. Vasyliv, A. Alexeev, Simulating incompressible flow on moving meshfree grids, *Comput. Fluids* 200 (2020) 104464. [doi:10.1016/j.compfluid.2020.104464](https://doi.org/10.1016/j.compfluid.2020.104464).

[19] T. Matsuda, K. Tsukui, S. Ii, A particle-based method using the mesh-constrained discrete point approach for two-dimensional Stokes flows, *Mech. Eng. J.* 9 (5) (2022) 22–00204. [doi:10.1299/mej.22-00204](https://doi.org/10.1299/mej.22-00204).

[20] T. Matsuda, S. Ii, A mesh-constrained discrete point method for incompressible flows with moving boundaries, *J. Comput. Phys.* 532 (2025) 113945. [doi:10.1016/j.jcp.2025.113945](https://doi.org/10.1016/j.jcp.2025.113945).

[21] P. Lancaster, K. Salkauskas, Surfaces generated by moving least squares methods, *Math. Comput.* 37 (155) (1981) 141–158. [doi:10.1090/S0025-5718-1981-0616367-1](https://doi.org/10.1090/S0025-5718-1981-0616367-1).

[22] T. Matsunaga, S. Koshizuka, Stabilized LSMPs method for complex free-surface flow simulation, *Comput. Methods Appl. Mech. Eng.* 389 (2022) 114416. [doi:10.1016/j.cma.2021.114416](https://doi.org/10.1016/j.cma.2021.114416).

[23] T. Matsunaga, High-order time-marching schemes for incompressible flow in particle methods, *Comput. Methods Appl. Mech. Eng.* 447 (2025) 118395. [doi:10.1016/j.cma.2025.118395](https://doi.org/10.1016/j.cma.2025.118395).

[24] J. A. Hopman, D. Santos, À. Alsalti-Baldellou, J. Rigola, F. X. Trias, Quantifying the checkerboard problem to reduce numerical dissipation, *J. Comput. Phys.* 521 (2025) 113537. [doi:10.1016/j.jcp.2024.113537](https://doi.org/10.1016/j.jcp.2024.113537).

[25] J. W. Swegle, S. W. Attaway, M. W. Heinstein, F. J. Mello, D. L. Hicks, An analysis of smoothed particle hydrodynamics, Tech. Rep. SAND-93-2513, Sandia National Labs., Albuquerque, NM (United States) (Feb. 1994). [doi:10.2172/10159839](https://doi.org/10.2172/10159839).

[26] S. Liu, X. He, Y. Guo, Y. Chang, W. Wang, A Dual-Particle Approach for Incompressible SPH Fluids, *ACM Trans. Graph.* 43 (3) (2024) 28:1–28:18. [doi:10.1145/3649888](https://doi.org/10.1145/3649888).

[27] C. T. Dyka, R. P. Ingel, An approach for tension instability in smoothed particle hydrodynamics (SPH), *Comput. Struct.* 57 (4) (1995) 573–580. [doi:10.1016/0045-7949\(95\)00059-P](https://doi.org/10.1016/0045-7949(95)00059-P).

[28] P. W. Randles, L. D. Libersky, Normalized SPH with stress points, *Int. J. Numer. Methods Eng.* 48 (10) (2000) 1445–1462. [doi:10.1002/1097-0207\(20000810\)48:10<1445::AID-NME831>3.0.CO;2-9](https://doi.org/10.1002/1097-0207(20000810)48:10<1445::AID-NME831>3.0.CO;2-9).

[29] C. M. Chalk, M. Pastor, J. Peakall, D. J. Borman, P. A. Sleigh, W. Murphy, R. Fuentes, Stress-Particle Smoothed Particle Hydrodynamics: An application to the failure and post-failure behaviour of slopes, *Comput. Methods Appl. Mech. Eng.* 366 (2020) 113034. [doi:10.1016/j.cma.2020.113034](https://doi.org/10.1016/j.cma.2020.113034).

[30] X. He, N. Liu, G. Wang, F. Zhang, S. Li, S. Shao, H. Wang, Staggered meshless solid-fluid coupling, *ACM Trans. Graph.* 31 (6) (2012) 149:1–149:12. [doi:10.1145/2366145.2366168](https://doi.org/10.1145/2366145.2366168).

[31] X. He, H. Wang, G. Wang, H. Wang, E. Wu, A Variational Staggered Particle Framework for Incompressible Free-Surface Flows (Jan. 2020). [arXiv:2001.09421](https://arxiv.org/abs/2001.09421), [doi:10.48550/arXiv.2001.09421](https://doi.org/10.48550/arXiv.2001.09421).

[32] S.-K. Park, G. Jo, H. J. Choe, Existence and stability in the virtual interpolation point method for the Stokes equations, *J. Comput. Phys.* 307 (2016) 535–549. [doi:10.1016/j.jcp.2015.12.002](https://doi.org/10.1016/j.jcp.2015.12.002).

[33] N. Trask, M. Perego, P. Bochev, A high-order staggered meshless method for elliptic problems, *SIAM J. Sci. Comput.* 39 (2) (2017) A479–A502. [doi:10.1137/16M1055992](https://doi.org/10.1137/16M1055992).

[34] N. Trask, M. Maxey, X. Hu, A compatible high-order meshless method for the Stokes equations with applications to suspension flows, *J. Comput. Phys.* 355 (2018) 310–326. [doi:10.1016/j.jcp.2017.10.039](https://doi.org/10.1016/j.jcp.2017.10.039).

[35] A. J. Chorin, Numerical solution of the Navier-Stokes equations, *Math. Comput.* 22 (104) (1968) 745–762. [doi:10.1090/S0025-5718-1968-0242392-2](https://doi.org/10.1090/S0025-5718-1968-0242392-2).

[36] F. Xiao, A Simple CIP Finite Volume Method for Incompressible Flows, *JSME Int. J. Ser. B Fluids Thermal Eng.* 47 (4) (2004) 664–671. [doi:10.1299/jsmeb.47.664](https://doi.org/10.1299/jsmeb.47.664).

[37] F. Xiao, A. Ikehata, T. Hasegawa, Numerical simulations of free-interface fluids by a multi-integrated moment method, *Computers & Structures* 83 (6) (2005) 409–423. [doi:10.1016/j.compstruc.2004.06.005](https://doi.org/10.1016/j.compstruc.2004.06.005).

[38] F. Xiao, R. Akoh, S. Ii, Unified formulation for compressible and incompressible flows by using multi-integrated moments II: Multi-dimensional version for compressible and incompressible flows, *Journal of Computational Physics* 213 (1) (2006) 31–56. [doi:10.1016/j.jcp.2005.08.002](https://doi.org/10.1016/j.jcp.2005.08.002).

[39] C. M. Rhie, W. L. Chow, Numerical study of the turbulent flow past an airfoil with trailing edge separation, *AIAA J.* 21 (11) (1983) 1525–1532. [doi:10.2514/3.8284](https://doi.org/10.2514/3.8284).

[40] S. Zhang, X. Zhao, S. Bayyuk, Generalized formulations for the Rhee–Chow interpolation, *J. Comput. Phys.* 258 (2014) 880–914. [doi:10.1016/j.jcp.2013.11.006](https://doi.org/10.1016/j.jcp.2013.11.006).

[41] F. H. Harlow, The particle-in-cell method for numerical solution of problems in fluid dynamics, *Tech. Rep. LADC-5288*, Los Alamos Scientific Lab., N. Mex. (Feb. 1962). [doi:10.2172/4769185](https://doi.org/10.2172/4769185).

[42] J. U. Brackbill, H. M. Ruppel, FLIP: A method for adaptively zoned, particle-in-cell calculations of fluid flows in two dimensions, *J. Comput. Phys.* 65 (2) (1986) 314–343. [doi:10.1016/0021-9991\(86\)90211-1](https://doi.org/10.1016/0021-9991(86)90211-1).

[43] X. K. Zhang, K.-C. Kwon, S.-K. Youn, The least-squares meshfree method for the steady incompressible viscous flow, *J. Comput. Phys.* 206 (1) (2005) 182–207. [doi:10.1016/j.jcp.2004.11.033](https://doi.org/10.1016/j.jcp.2004.11.033).

[44] B. Chandra, R. Hashimoto, S. Matsumi, K. Kamrin, K. Soga, Stabilized mixed material point method for incompressible fluid flow analysis, *Comput. Methods Appl. Mech. Eng.* 419 (2024) 116644. [doi:10.1016/j.cma.2023.116644](https://doi.org/10.1016/j.cma.2023.116644).

[45] K.-Y. He, Y.-F. Jin, X.-W. Zhou, Z.-Y. Yin, X. Chen, An improved MPM formulation for free surface flow problems based on finite volume method, *Comput. Methods Appl. Mech. Eng.* 446 (2025) 118264. [doi:10.1016/j.cma.2025.118264](https://doi.org/10.1016/j.cma.2025.118264).

[46] Y. Xu, G. Yang, Y. Zhu, D. Hu, A coupled SPH–FVM method for simulating incompressible interfacial flows with large density difference, *Eng. Anal. Bound. Elem.* 128 (2021) 227–243. [doi:10.1016/j.enganabound.2021.04.005](https://doi.org/10.1016/j.enganabound.2021.04.005).

[47] K. Nishiguchi, T. Shimada, C. Peco, K. Kondo, S. Okazawa, M. Tsubokura, Eulerian finite volume method using Lagrangian markers with reference map for incompressible fluid–structure interaction problems, *Comput. Fluids* 274 (2024) 106210. [doi:10.1016/j.compfluid.2024.106210](https://doi.org/10.1016/j.compfluid.2024.106210).

[48] H. A. van der Vorst, Bi-CGSTAB: A Fast and Smoothly Converging Variant of Bi-CG for the Solution of Nonsymmetric Linear Systems, *SIAM J. Sci. and Stat. Comput.* 13 (2) (1992) 631–644. [doi:10.1137/0913035](https://doi.org/10.1137/0913035).

[49] U. Ghia, K. N. Ghia, C. T. Shin, High-Re solutions for incompressible flow using the Navier-Stokes equations and a multigrid method, *J. Comput. Phys.* 48 (3) (1982) 387–411. [doi:10.1016/0021-9991\(82\)90058-4](https://doi.org/10.1016/0021-9991(82)90058-4).

[50] S. Hou, Q. Zou, S. Chen, G. Doolen, A. C. Cogley, Simulation of Cavity Flow by the Lattice Boltzmann Method, *J. Comput. Phys.* 118 (2) (1995) 329–347. [doi:10.1006/jcph.1995.1103](https://doi.org/10.1006/jcph.1995.1103).

[51] Y.-F. Peng, Y.-H. Shiau, R. R. Hwang, Transition in a 2-D lid-driven cavity flow, *Comput. Fluids* 32 (3) (2003) 337–352. [doi:10.1016/S0045-7930\(01\)00053-6](https://doi.org/10.1016/S0045-7930(01)00053-6).

[52] L. Li, J. F. Klausner, R. Mei, Flow structures in two-dimensional lid-driven cavity flow: Benchmark numerical results for steady flows, *Eur. J. Mech. B/Fluids* 114 (2025) 204313. [doi:10.1016/j.euromechflu.2025.204313](https://doi.org/10.1016/j.euromechflu.2025.204313).

[53] H. Düttsch, F. Durst, S. Becker, H. Lienhart, Low-Reynolds-number flow around an oscillating circular cylinder at low Keulegan–Carpenter numbers, *J. Fluid Mech.* 360 (1998) 249–271. [doi:10.1017/S002211209800860X](https://doi.org/10.1017/S002211209800860X).

[54] E. Guilméneau, P. Queutey, A NUMERICAL SIMULATION OF VORTEX SHEDDING FROM AN OSCILLATING CIRCULAR CYLINDER, *J. Fluid. Struct.* 16 (6) (2002) 773–794. [doi:10.1006/jfls.2002.0449](https://doi.org/10.1006/jfls.2002.0449).

[55] C. Chi, A. Abdelsamie, D. Thévenin, A directional ghost-cell immersed boundary method for incompressible flows, *J. Comput. Phys.* 404 (2020) 109122. [doi:10.1016/j.jcp.2019.109122](https://doi.org/10.1016/j.jcp.2019.109122).

[56] M. B. Ghomizad, H. Kor, K. Fukagata, A sharp interface direct-forcing immersed boundary method using the moving least square approximation, *J. Fluid Sci. Technol.* 16 (2) (2021) JFST0013–JFST0013. [doi:10.1299/jfst.2021jfst0013](https://doi.org/10.1299/jfst.2021jfst0013).